The Astrophysical Journal, 847:13 (17pp), 2017 September 20 https://doi.org/10.3847/1538-4357/aa88c9

Stellar Mass Function of Active and Quiescent Galaxies via the Continuity Equation

A. Lapi[1,2,3], C. Mancuso[2,4], A. Bressan[1,2,3], and L. Danese[1,2,3]
[1] SISSA, Via Bonomea 265, I-34136 Trieste, Italy
[2] INFN-Sezione di Trieste, via Valerio 2, I-34127 Trieste, Italy
[3] INAF-Osservatorio Astronomico di Trieste, via Tiepolo 11, I-34131 Trieste, Italy
[4] INAF-IRA, Via P. Gobetti 101, I-40129 Bologna, Italy
Received 2017 June 8; revised 2017 August 21; accepted 2017 August 24; published 2017 September 14

Abstract

The continuity equation is developed for the stellar mass content of galaxies and exploited to derive the stellar mass function of active and quiescent galaxies over the redshift range $z \sim 0$–8. The continuity equation requires two specific inputs gauged from observations: (i) the star formation rate functions determined on the basis of the latest UV+far-IR/submillimeter/radio measurements and (ii) average star formation histories for individual galaxies, with different prescriptions for disks and spheroids. The continuity equation also includes a source term taking into account (dry) mergers, based on recent numerical simulations and consistent with observations. The stellar mass function derived from the continuity equation is coupled with the halo mass function and with the SFR functions to derive the star formation efficiency and the main sequence of star-forming galaxies via the abundance-matching technique. A remarkable agreement of the resulting stellar mass functions for active and quiescent galaxies of the galaxy main sequence, and of the star formation efficiency with current observations is found; the comparison with data also allows the characteristic timescales for star formation and quiescence of massive galaxies, the star formation history of their progenitors, and the amount of stellar mass added by in situ star formation versus that contributed by external merger events to be robustly constrained. The continuity equation is shown to yield quantitative outcomes that detailed physical models must comply with, that can provide a basis for improving the (subgrid) physical recipes implemented in theoretical approaches and numerical simulations, and that can offer a benchmark for forecasts on future observations with multiband coverage, as will become routinely achievable in the era of *JWST*.

Key words: galaxies: evolution – galaxies: high-redshift – galaxies: luminosity function, mass function – galaxies: star formation – galaxies: statistics

1. Introduction

Some recent findings have significantly rekindled interest in the field of galaxy formation and evolution. The first concerns the discovery of an abundant population of dusty star-forming galaxies at redshifts $z \gtrsim 1$, which has been shown to be responsible for the bulk of the cosmic star formation history, in particular around the crucial redshifts $z \approx 2$–3 where it peaks (e.g., Gruppioni et al. 2013; Rowan-Robinson et al. 2016; Bourne et al. 2017; Dunlop et al. 2017; Lapi et al. 2017; Novak et al. 2017), and to be present even out to $z \lesssim 6$ (e.g., Cooray et al. 2014; Riechers et al. 2017; Zavala et al. 2017). Such achievement has become feasible only recently thanks to wide-area far-IR/submillimeter surveys conducted by *Herschel*, ASTE/AzTEC, APEX/LABOCA, JCMT/SCUBA-2, and ALMA-SPT (e.g., Lapi et al. 2011; Gruppioni et al. 2013, 2015; Weiss et al. 2013; Koprowski et al. 2014, 2016; Strandet et al. 2016), in many instances made easier by gravitational lensing from foreground objects (e.g., Negrello et al. 2014, 2017; Nayyeri et al. 2016). In fact, galaxies endowed with star formation rates $\dot{M}_\star \gtrsim$ a few tens $M_\odot\,\mathrm{yr}^{-1}$ at redshift $z \gtrsim 2$ were largely missed by rest-frame optical/UV surveys because of heavy dust obscuration, which is difficult to correct for with standard techniques based only on UV spectral data (e.g., Bouwens et al. 2016, 2017; Mancuso et al. 2016a; Ikarashi et al. 2017; Pope et al. 2017; Simpson et al. 2017).

High-resolution, follow-up observations of these galaxies in the far-IR/submillimeter/radio band via ground-based interferometers, such as SMA, VLA, PdBI, and recently ALMA, have revealed star formation to occur in a few collapsing clumps distributed over spatial scales smaller than a few kiloparsecs (see Ikarashi et al. 2015; Simpson et al. 2015; Straatman et al. 2015; Barro et al. 2016; Spilker et al. 2016; Tadaki et al. 2017). A strongly baryon-dominated stellar core with high ongoing SFR is often surrounded out to $\lesssim$15 kpc by a clumpy, unstable gaseous disk in nearly Keplerian rotation (e.g., Genzel et al. 2017; Swinbank et al. 2017).

Observations of dusty star-forming galaxies in the optical and near/mid-IR band from the *Spitzer Space Telescope* (*SST*), *WISE*, and *Hubble Space Telescope* (*HST*) have allowed their stellar mass content to be characterized. The vast majority feature stellar masses strongly correlated with the SFR, in the way of an almost linear relationship dubbed the "Main Sequence," with a normalization steadily increasing as a function of redshift and a limited scatter around 0.25 dex (see Daddi et al. 2007; Rodighiero et al. 2011, 2015; Speagle et al. 2014; Whitaker et al. 2014; Renzini & Peng 2015; Salmon et al. 2015; Tasca et al. 2015; Kurczynski et al. 2016; Tomczak et al. 2016; Bourne et al. 2017; Dunlop et al. 2017; Schreiber et al. 2017).

Another relevant piece of news concerns the discovery by deep near-IR surveys of an increasing number of massive galaxies, $M_\star \gtrsim$ several $10^{10}\,M_\odot$, at high redshifts $z \gtrsim 2$ (see Bernardi et al. 2013, 2017; Ilbert et al. 2013; Duncan et al. 2014; Tomczak et al. 2014; Caputi et al. 2015; Grazian et al. 2015; Song et al. 2016; Thanjavur et al. 2016; Davidzon et al. 2017). Even more interesting, some of them are found to be already in passive evolution at $z \gtrsim 2$–3 and to feature chemical properties similar to local early-type galaxies, including a (super)solar metallicity and a pronounced

α-enhancement. There is the intriguing yet still debated possibility that the dusty star-forming objects seen in the far-IR/submillimeter band constitute the progenitors of the massive (quiescent) galaxies increasingly detected at high redshifts via deep near-IR surveys (Straatman et al. 2014, 2016; Lonoce et al. 2015; Kriek et al. 2016; Mawatari et al. 2016; Michalowski et al. 2016; Davidzon et al. 2017; Glazebrook et al. 2017).

Relevant model-independent information on the cosmic star formation and mass growth history can be inferred by comparing the observed SFR function, stellar mass function, and main sequence for active and quiescent galaxies (e.g., Leja et al. 2015; Contini et al. 2017; Mancuso et al. 2016a, 2016b; Tomczak et al. 2016; Steinhardt et al. 2017). This procedure can provide stringent constraints, e.g., on the typical timescales for star formation and quiescence, on the overall star formation efficiency, on the initial mass function (IMF), and on the amount of stellar mass added by in situ star formation versus that contributed by external merger events. Such outcomes can also be helpful to improve the (subgrid) physical recipes implemented in theoretical models and numerical simulations, which currently face some difficulties in reproducing the observed abundances of strongly star-forming and massive quiescent galaxies at $z \gtrsim 2$–3 (e.g., Wellons et al. 2015; Behroozi & Silk 2017; Davé et al. 2017; Furlong et al. 2017; Hopkins et al. 2017; Rong et al. 2017).

In the present paper, we pursue the above strategy for the first time in a *quantitative* way, by exploiting the specific tool constituted by the "continuity equation." Originally devised to connect quasar statistics to the demographics of supermassive black hole relics (Cavaliere et al. 1971; Soltan 1982; Small & Blandford 1992; Salucci et al. 1999; Marconi et al. 2004; Yu & Lu 2004, 2008; Merloni & Heinz 2008; Shankar et al. 2009, 2013; Aversa et al. 2015), here we develop it for the stellar mass content of galaxies in order to derive the stellar mass function of active and passive galaxies at different redshifts from the SFR functions and average star formation histories for individual objects. Our approach includes a source term in the continuity equation that takes into account dry mergers and tidal stripping effects, based on observations and on state-of-the-art numerical simulations. With the term "dry mergers" we refer to events that add the entire mass content of stars in the merging objects without contributing significantly to in situ star formation; starbursts triggered by wet mergers, although included as star-forming objects populating the SFR functions, are expected to contribute little to the final stellar mass, and especially so for massive galaxies.

Moreover, we will exploit the abundance-matching technique to derive the star formation efficiency and the main sequence of star-forming galaxies, and compare the outcome to recent observational determinations. Specifically, we will demonstrate via the continuity equation that the dusty, strongly star-forming galaxies at $z \gtrsim 2$ are indeed the progenitors of massive quiescent galaxies, and that the latter's mass growth is dominated by in situ star formation with an overall efficiency of less than 20%.

The plan of this paper is straightforward. In Section 2, we describe the basic ingredients of our analysis: the SFR functions and the adopted star formation histories for individual galaxies; in Section 3, we solve the continuity equation for the stellar mass function of active and passive galaxies, and describe how to derive from those the star formation efficiency and the main sequence of star-forming galaxies; in Section 4, we present our results and compare them to observations, discussing the relevant implications for galaxy formation and evolution; and in Section 5, we summarize our findings.

Throughout this work, we adopt the standard flat cosmology (Planck Collaboration XIII 2016) with round parameter values: matter density $\Omega_M = 0.32$, baryon density $\Omega_b = 0.05$, Hubble constant $H_0 = 100\,h\,\mathrm{km\,s^{-1}\,Mpc^{-1}}$ with $h = 0.67$, and mass variance $\sigma_8 = 0.83$ on a scale of $8\,h^{-1}\,\mathrm{Mpc}$. Stellar masses and SFRs (or luminosities) of galaxies are evaluated assuming the Chabrier (2003) IMF.

2. Basic Ingredients

Our analysis relies on two basic ingredients: (i) an observational determination of the SFR function at different redshifts and (ii) deterministic evolutionary tracks describing the average star formation history of individual galaxies. In this section, we recall the notions relevant to the investigation of the stellar mass function, referring the reader to the papers by Mancuso et al. (2016a, 2016b) and Lapi et al. (2017) for more details.

2.1. SFR Functions and Cosmic SFR Density

The first ingredient is composed of the intrinsic SFR function $dN/d\log\dot{M}_\star$, namely, the number density of galaxies per logarithmic bin of the SFR $[\log\dot{M}_\star, \log\dot{M}_\star + d\log\dot{M}_\star]$ at a given redshift z. This has been accurately determined by Mancuso et al. (2016a, 2016b) and Lapi et al. (2017) by exploiting the most recent determinations of the evolving galaxy luminosity functions from (dust-corrected) UV, far-IR, submillimeter, and radio data.

The SFR function can be described as a smooth Schechter function,

$$\frac{dN}{d\log\dot{M}_\star}(\dot{M}_\star, z) = \mathcal{N}(z)\left[\frac{\dot{M}_\star}{\dot{M}_{\star,c}(z)}\right]^{1-\alpha(z)} e^{-\dot{M}_\star/\dot{M}_{\star,c}(z)}, \quad (1)$$

with three parameters: the overall normalization $\mathcal{N}$, the characteristic SFR $\dot{M}_{\star,c}$, and the faint-end slope α. The redshift evolution of each parameter was measured via an educated fit to the observed data in unitary redshift bins by Mancuso et al. (2016a, 2016b). As extensively discussed by the latter authors, the SFR function is mainly determined by (dust-corrected) UV data for SFR $\dot{M}_\star \lesssim 30\,M_\odot\,\mathrm{yr^{-1}}$ since in this range dust emission is mainly due to the diffuse (cirrus) dust component, and standard UV dust corrections based on the UV slope are reliable (see Meurer et al. 1999; Calzetti et al. 2000; Bouwens et al. 2015, 2016, 2017); here we use the Meurer/Calzetti extinction law, but note that switching to a Small Magellanic Cloud (SMC) extinction law mildly affects the SFR function at the faint end (see also Section 4 and Figure 6). On the other hand, the SFR function is mainly determined by far-IR/submillimeter/radio data for SFRs $\dot{M}_\star \gtrsim 10^2\,M_\odot\,\mathrm{yr^{-1}}$ since in this range dust emission is largely dominated by molecular clouds, and UV corrections are wildly dispersed and statistically fail (see Silva et al. 1998; Efstathiou et al. 2000; Coppin et al. 2015; Reddy et al. 2015; Fudamoto et al. 2017).

The resulting SFR functions at representative redshifts are illustrated along with the relevant data collection in Figure 1. In

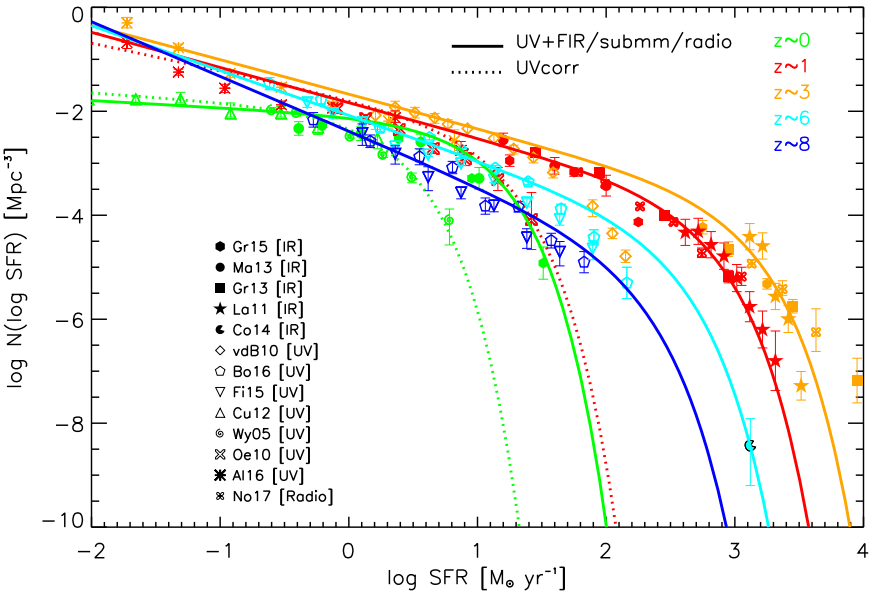

Figure 1. SFR functions at redshifts $z = 0$ (green), 1 (red), 3 (orange), and 6 (blue) determined using the procedure of Mancuso et al. (2016a, 2016b) and Lapi et al. (2017). Solid lines refer to the rendition from UV plus far-IR/submillimeter/radio data; dotted lines (only plotted at $z \approx 0$ and 1) refer to the rendition from UV data (dust corrected according to standard prescriptions based on the UV slope). UV data (open symbols) are from van der Burg et al. (2010; diamonds), Bouwens et al. (2016, 2017; pentagons), Finkelstein et al. (2015; inverted triangles), Cucciati et al. (2012; triangles), Wyder et al. (2005; spirals), Oesch et al. (2010; crosses), and Alavi et al. (2016; asterisks); far-IR/submillimeter data are from Gruppioni et al. (2015; hexagons), Magnelli et al. (2013; circles), Gruppioni et al. (2013; squares), Lapi et al. (2011; stars), and Cooray et al. (2014; Pacmans); and radio data are from Novak et al. (2017; clovers).

Mancuso et al. (2016a, 2016b, 2017) and Lapi et al. (2017), we validated them against independent data sets, including integrated galaxy number counts at significant far-IR/submillimeter/radio wavelengths, counts/redshift distributions of strongly gravitationally lensed galaxies, main sequence of star-forming galaxies and AGNs, redshift evolution of the cosmic SFR, and high-redshift observables including the history of cosmic reionization.

All in all, our determination of the SFR functions implies a significant number density of dusty star-forming galaxies with SFR $\dot{M}_\star \gtrsim 10^2\, M_\odot\,\mathrm{yr}^{-1}$, currently missed by (dust-corrected) UV data. To highlight this point more clearly, in Figure 1 we also report at $z \lesssim 1$ the SFR function that would have been inferred based solely on UV data, dust corrected via the UV slope. The UV data considerably underestimate the SFR function for SFRs $\dot{M}_\star \gtrsim 30\, M_\odot\,\mathrm{yr}^{-1}$ because of strong dust extinction. Interestingly, the shape of the SFR function for $\dot{M}_\star \gtrsim 10^2\, M_\odot\,\mathrm{yr}^{-1}$, which so far has been probed only indirectly at $z \gtrsim 4$ due to sensitivity limits in current wide-area far-IR surveys, is found to agree out to $z \lesssim 6$ with the constraints from the recent VLA-COSMOS radio survey (Novak et al. 2017) and from the few individual galaxies detected at $z \gtrsim 5$ with ALMA and SMA (e.g., Riechers et al. 2017; Zavala et al. 2017). We will demonstrate via the continuity equation that a robust probe on the bright end of the SFR function at high redshift $z \gtrsim 4$ is provided by the galaxy stellar mass function.

For the analysis in the present paper, we shall assume that at $z \gtrsim 1$, active galaxies populate the total (UV+far-IR/submillimeter/radio) SFR function and feature a spheroid-like star formation history; the latter envisages a nearly constant behavior of the SFR as a function of galaxy age, with a timescale of $\lesssim$1 Gyr at high SFR $\dot{M}_\star \gtrsim 30\, M_\odot\,\mathrm{yr}^{-1}$, increasing to a few gigayears for lower SFRs (see Section 2.2 for details). At high SFRs, such a population comprises dusty star-forming, far-IR-/submillimeter-selected galaxies, which will turn out to be the progenitors of local massive dead spheroids with masses $M_\star \gtrsim$ a few $10^{10}\, M_\odot$; at low SFRs, it comprises mildly obscured, UV-selected galaxies (e.g., Lyman break galaxies) that will end up in objects with stellar masses $M_\star \lesssim 10^{10}\, M_\odot$.

At $z \lesssim 1$, we will show that a bimodal star formation history is required. On the one hand, the bright end of the total (UV+far-IR/submillimeter/radio) SFR function is assumed to be populated by galaxies with the same spheroid-like star formation history sketched above; since the knee of the SFR function toward $z \sim 0$ recedes a lot, the star formation timescales are on average appreciably longer than those at $z \sim 1$, attaining up to a few gigayears (possibly split in many recurrent, shorter bursts); this population comprises a mixed bag of objects, including low-mass spheroids (e.g., bulges), irregulars, and reactivations of massive galaxies. On the other hand, the UV-inferred SFR function is assumed to be populated by galaxies with a disk-like star formation history, i.e., exponentially declining SFR as a function of galaxy age with long timescales of several gigayears (see also Cai et al. 2013, 2014); these objects will end up in disk-dominated galaxies with stellar masses $M_\star \lesssim$ several $10^{10}\, M_\odot$. In Section 2.2, we will describe in detail the adopted spheroid-like or disk-like star formation histories for individual galaxies.

From the SFR function, we can straightforwardly compute the cosmic SFR density as

$$\rho_{\rm SFR}(z) = \int d\log \dot{M}_\star \, \frac{dN}{d\log \dot{M}_\star}\, \dot{M}_\star\,, \qquad (2)$$

integrated down to a limit $\dot{M}_\star \lesssim 10^{-1}\, M_\odot\,\mathrm{yr}^{-1}$ for fair comparison to observational data, in particular with current blank-field UV surveys at high $z \gtrsim 4$; the outcome is illustrated in Figure 2. The result from the (dust-corrected) UV-inferred SFR functions is in good agreement with the UV data by Schiminovich et al. (2005) at $z \lesssim 4$ and by Bouwens et al. (2015, 2016, 2017) at $z \gtrsim 4$. It also agrees with the estimate by

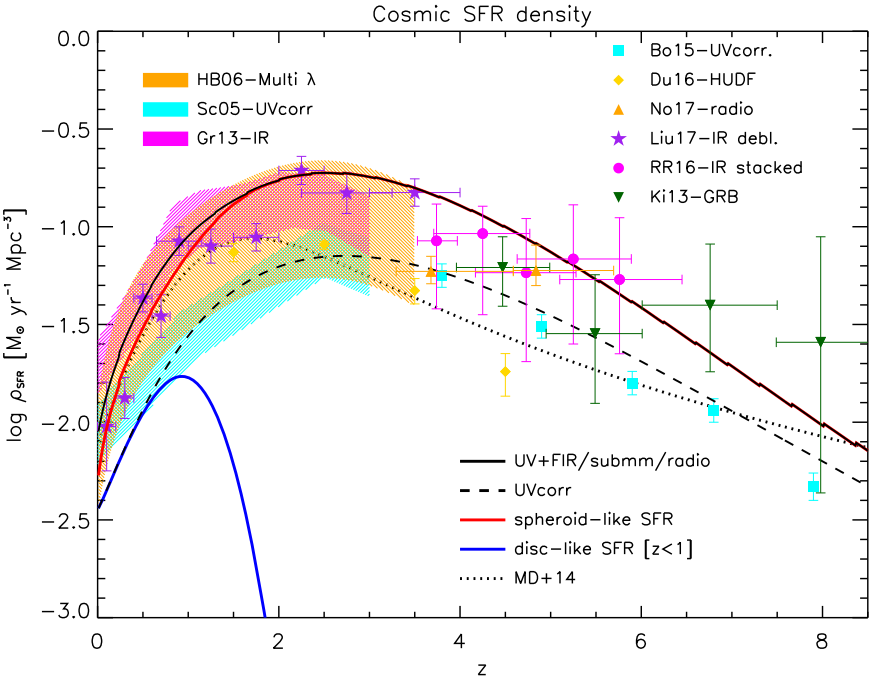

Figure 2. Cosmic SFR density as a function of redshift. The black solid line is the density derived from integrating the total (UV+far-IR/submillimeter/radio) SFR functions of Figure 1 down to a limit $\dot{M}_\star \sim 10^{-1}\,M_\odot\,\mathrm{yr}^{-1}$. The contributions from objects with spheroid-like and disk-like star formation histories (see Section 2) are highlighted by the red and blue solid lines, respectively. The black dashed line illustrates the SFR density when basing on the (dust-corrected) UV-inferred SFR functions at any redshift. For reference, the dotted line illustrates the determination by Madau & Dickinson (2014). Data are from (dust-corrected) UV observations by Schiminovich et al. (2005; cyan shaded area) and Bouwens et al. (2015; cyan squares); ALMA submillimeter observations of UV-selected galaxies on the HUDF by Dunlop et al. (2017); VLA radio observations on the COSMOS field by Novak et al. (2017); multiwavelength determination including UV, radio, Hα, and mid-IR 24 μm data collected by Hopkins & Beacom (2006; orange shaded area); *Herschel* far-IR observations by Gruppioni et al. (2013 magenta shaded area); *Herschel* far-IR stacking by Rowan-Robinson (2016; magenta circles); far-IR/sub-mm observations from deblended data on the GOODS field by Liu et al. (2017); and estimates from long GRB rates by Kistler et al. (2009; 2013; green stars).

ALMA observations of UV-selected galaxies in the HUDF (see Dunlop et al. 2017); this is because the rather small area of the HUDF survey allows only moderately star-forming galaxies with mild dust obscuration to be picked up, on which the UV slope-based corrections still work pretty well.

However, the cosmic SFR density from (dust-corrected) UV data is inconsistent with other data sets both at low and high redshifts. Specifically, at redshifts $z \lesssim 4$, it falls short with respect to the multiwavelength determination by Hopkins & Beacom (2006) based on UV/optical, radio, Hα, and mid-IR 24 μm data; to the far-IR measurements from *Herschel* by Magnelli et al. (2013) and Gruppioni et al. (2013); and to the recent estimate from deblended data from *Herschel*, JCMT/AzTEC, and JCMT/SCUBA-2 in the GOODS field by Liu et al. (2017). At redshifts $z \gtrsim 4$, it underestimates the determinations based on stacking of far-IR data from *Herschel* by Rowan-Robinson et al. (2016), the measurements from radio data by Novak et al. (2017), and the estimates based on long GRB rates from *Swift* by Kistler et al. (2009, 2013). This mostly reflects the fact, already mentioned above, that the UV-inferred SFR functions (even corrected for dust extinction via the UV slope) appreciably underestimate the number density of dusty galaxies with $\dot{M}_\star \gtrsim 30\,M_\odot\,\mathrm{yr}^{-1}$.

The agreement with all of these data sets is substantially improved when basing on the cosmic SFR density computed from the UV+far-IR/submillimeter/radio SFR functions. We also illustrate the contribution from objects with spheroid-like and disk-like star formation histories to the total density. We remark that at $z \gtrsim 1$ most of the SFR density is contributed by the dusty star-forming progenitors of local massive quiescent spheroids, while at $z \lesssim 1$ it is contributed by both disk-dominated galaxies and low-mass spheroids, irregulars, and reactivated massive galaxies.

2.2. Star Formation History of Individual Galaxies

The second ingredient of our analysis is composed of the deterministic evolutionary tracks for the history of star formation in individual galaxies. The relevant quantity $\dot{M}_\star(\tau|M_\star, t)$ is the behavior of the SFR as a function of the internal galactic age τ (i.e., the time since the beginning of significant star formation activity) for a galaxy with relic stellar mass $M_\star$ at cosmological time t (corresponding to redshift z).

For high $z \gtrsim 1$ strongly star-forming galaxies (that will turn out to be the progenitors of local dead massive spheroids), many SED-modeling studies (e.g., Papovich et al. 2011; Smit et al. 2012; Moustakas et al. 2013; Steinhardt et al. 2014; Cassará et al. 2016; Citro et al. 2016) suggest a slow power-law increase of the SFR $\dot{M}_\star \propto \tau^\kappa$ with $\kappa \lesssim 1$ over a timescale $\tau_{\rm sphe} \lesssim$ gigayear, then followed by a rapid quenching, at least for massive objects. For the sake of simplicity (see Section 3), here we adopt the law

$$\dot{M}_\star(\tau|M_\star, t) = \frac{\kappa+1}{1-\mathcal{R}}\,\frac{M_\star}{\tau_{\rm sphe}}(\tau/\tau_{\rm sphe})^\kappa\,\Theta_{\rm H}[\tau \leqslant \tau_{\rm sphe}], \quad (3)$$

where $\Theta(\cdot)$ is the Heaviside step function. The quantity $\mathcal{R}$ is the fraction of mass restituted to the interstellar medium by massive stars, computed in the instantaneous recycling

approximation; for a Chabrier IMF and star formation timescales $\lesssim$ gigayear, $\mathcal{R} \approx 0.4$ applies.

As to the parameters involved in the above expressions, recent observations by ALMA have shown that in high-redshift galaxies, star formation occurred within a compact region $\lesssim$ a few kiloparsecs over timescales $\tau_{\rm sphe} \lesssim 0.5$–1 Gyr at violent rates $\dot{M}_\star \gtrsim$ a few $10^2\,M_\odot\,{\rm yr}^{-1}$ under heavily dust-enshrouded conditions (e.g., Scoville et al. 2014, 2016; Ikarashi et al. 2015; Simpson et al. 2015; Straatman et al. 2015; Spilker et al. 2016; Tadaki et al. 2017). The duration of the main star formation episode $\tau_{\rm sphe} \lesssim 0.5$–1 Gyr in high-redshift dusty star-forming galaxies, which are the candidate progenitors of massive spheroids, is also confirmed by local observations of the α-enhancement, i.e., iron underabundance compared to α elements. This occurs because star formation is stopped, presumably by some form of energetic feedback (e.g., due to the central supermassive black hole), before type SN Ia explosions can pollute the interstellar medium with substantial amounts of iron (e.g., Romano et al. 2002; Thomas et al. 2005; Gallazzi et al. 2006; for a review, see Renzini 2006). On the contrary, in low-mass spheroidal galaxies with $M_\star \lesssim 10^{10}\,M_\odot$, data on the age of the stellar population and chemical abundances indicate that star formation proceeded for longer times, mainly regulated by supernova feedback and stellar winds (see review by Conroy 2013).

On this basis, we parameterize the timescale for the duration of the main SFR episode in objects with a spheroid-like star formation history as a function of the peak SFR value $\dot{M}_\star(\tau_{\rm sphe}|M_\star, t) = (\kappa + 1)M_\star/(1 - \mathcal{R})\tau_{\rm sphe}$ via the implicit equation

$$\tau_{\rm sphe} = \frac{\tau^+_{\rm sphe} + \tau^-_{\rm sphe}}{2} + \frac{\tau^+_{\rm sphe} - \tau^-_{\rm sphe}}{2}\tanh\left[\frac{\dot{M}_\star(\tau_{\rm sphe}|M_\star, t)}{5\,M_\odot{\rm yr}^{-1}}\right],$$
$$\tau^+_{\rm sphe} = 0.6\ {\rm Gyr}\left(\frac{1+z}{3}\right)^{-3/2}, \quad \tau^-_{\rm sphe} = t_z; \tag{4}$$

this has to be solved on a grid of $M_\star$ and t (or z; see details in Section 3). The $\tanh(\cdot)$ function interpolates smoothly between the short timescale $\tau^+_{\rm sphe} \lesssim 1$ Gyr for high star-forming galaxies and a long timescale $\tau^-_{\rm sphe} \sim t_z$ of the order of the cosmic time for galaxies with low SFRs. Note that in $\tau^+_{\rm sphe}$ the dependence on redshift matches that of the dynamical time $\propto 1/\sqrt{G\,\rho} \propto (1+z)^{-3/2}$, in turn following the increase in average density $\rho \propto (1+z)^3$ of the ambient medium. Our results will be insensitive to the specific shape of the smoothing function. With a similar parameterization, Mancuso et al. (2016b) were able to reproduce the main sequence of star-forming galaxies at $z \approx 2$. We recall that at $z \lesssim 1$, since the knee of the SFR functions recedes a lot, most of the objects with spheroid-like star formation histories are characterized by moderate SFR $\dot{M}_\star \lesssim 10\,M_\odot\,{\rm yr}^{-1}$, and hence rather long star formation timescales up to a few gigayears (see Figure 3, bottom panel).

As to the quenching timescale, the observed fraction of far-IR-detected host galaxies in X-ray (e.g., Mullaney et al. 2012; Page et al. 2012; Rosario et al. 2012; Barger et al. 2015; Stanley et al. 2015; Harrison et al. 2016) and optically selected AGNs (e.g., Mor et al. 2012; Wang et al. 2013; Willott et al. 2015; Xu et al. 2015; Harris et al. 2016; Netzer et al. 2016) points toward an SFR abruptly stopping, at least in massive galaxies, after $\tau_{\rm sphe}$ over a short timescale $\lesssim 10^8$ yr due to the action of feedback (see Lapi et al. 2014). To avoid introducing an additional parameter, in Equation (3) we truncate the SFR abruptly after $\tau^+_{\rm sphe}$; we checked that an exponential quenching over a short timescale $\lesssim \tau^+_{\rm sphe}/\zeta$ with $\zeta \gtrsim$ a few will add an additional small delay and produce very similar outcomes in the stellar mass function.

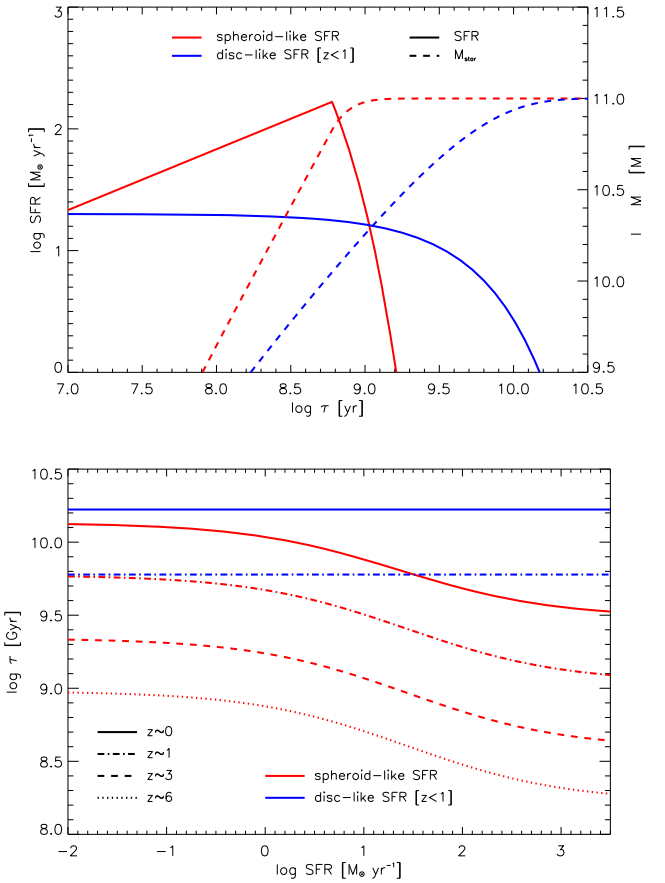

Figure 3. Top panel: evolution of the SFR (solid lines, left y-axis) andthe stellar mass (dashed lines, right y-axis) as a function of the galactic age τ for spheroid-like (see Equation (3); red lines) and disk-like (see Equation (5); blue lines) star formation histories; both evolutions refer to a galaxy with final stellar mass $M_\star \approx 10^{11}\,M_\odot$. Bottom panel: the star formation timescales $\tau_{\rm sphe}$ for spheroid-like (see Equation (4); red lines) and disk-like objects (only plotted at $z \lesssim 1$, see Equation (5); blue lines) as a function of the SFR and at redshift $z \approx 0$ (solid), 1 (dotted–dashed), 3 (dashed), and 6 (dotted).

On the other hand, in low redshift $z \lesssim 1$ disk-dominated galaxies, it is well known that on average, star formation declines exponentially as a function of the galactic age, with a long characteristic timescale of several gigayears; for example, for our Milky Way, it amounts to ≈6–7 Gyr (see Chiappini et al. 1997; Courteau et al. 2014; Pezzulli & Fraternali 2016). In view of these classic evidences, we adopt

$$\dot{M}_\star(\tau|M_\star, t) = \frac{1}{1-\mathcal{R}}\,\frac{M_\star}{\tau_{\rm disc}}\,e^{-\tau/\tau_{\rm disc}},$$
$$\tau_{\rm disc} = 6\ {\rm Gyr}\left(\frac{1+z}{2}\right)^{-3/2}. \tag{5}$$

In Figure 3 (top panel), we illustrate an example of the resulting spheroid-like and disk-like star formation histories; the relative star formation timescales as a function of SFR and cosmic time

are also shown (bottom panel). For both disk- and spheroid-like histories, we assume a dispersion of 0.25 dex around the average star formation timescales; this value is inspired by the scatter observed in the specific SFRs $\dot{M}_\star/M_\star$ (the inverse of a mass doubling time) of active galaxies at different redshifts (e.g., Madau & Dickinson 2014), and it will turn out to produce the observed dispersion in the resulting star formation main sequence (see Section 4 and Figure 10).

We caution the reader that in the literature there have been attempts to parameterize with a unique shape the average star formation history of galaxies. A classic way involves the so-called "delayed exponential" model $\dot{M}_\star(\tau) \propto \tau^\kappa\, e^{-\tau/\tau_\star}$ with two parameters κ and $\tau_\star$ controlling the early power-law rise and the late exponential decline. More recently, analogy with the behavior of the cosmic SFR density (see Gladders et al. 2013) and indications from numerical simulations (see Diemer et al. 2017) have suggested a log-normal shape $\dot{M}_\star(\tau) \propto e^{-(\ln\tau/\tau_\star)^2/2\sigma_\star^2}\Big/\sqrt{2\pi\sigma_\star^2}\;\tau$ with the parameters $\tau_\star$ and $\sigma_\star$ controlling peak time and width. Other descriptions with a more complex parametric form have also been proposed based on observations (e.g., Leitner & Kravtsov 2011) or empirical models (e.g., Behroozi et al. 2013; Moster et al. 2013). All of these shapes can be useful to describe the star formation history averaged over the entire population of a galaxy survey; however, chemical and photometric data require differentiating between disk-like and spheroid-like star formation histories, making the parametric models for each class (e.g., see Figure 2 in Diemer et al. 2017) essentially indistinguishable from our simple adopted shapes. For example, to describe the history of a star-forming disk, the timescale of the early rise has to be much faster than that of the late decline to mirror the exponential model of Equation (5); on the contrary, in a massive spheroid progenitor, the SFR must be nearly constant and then abruptly quenched to mirror the power-law truncated model of Equation (3).

3. The Continuity Equation

The continuity equation was originally devised to connect the AGN statistics to the demographics of both active and dormant supermassive black holes (Cavaliere et al. 1971; Soltan 1982; Small & Blandford 1992; Salucci et al. 1999; Marconi et al. 2004; Yu & Lu 2004, 2008; Merloni & Heinz 2008; Shankar et al. 2009, 2013). Aversa et al. (2015) were the first to show that it can be also applied to the stellar component in galaxies to link the evolution across cosmic times of the SFR function to the stellar mass functions. The continuity equation in integral formulation is written

$$\frac{dN}{d\log\dot{M}_\star}(\dot{M}_\star, t) = \int d\log M_\star\, \partial_t\Bigg[\frac{dN}{d\log M_\star}(M_\star, t) - S(M_\star, t)\Bigg]\frac{d\tau}{d\log\dot{M}_\star}(\dot{M}_\star|M_\star, t)\;; \tag{6}$$

here, the term on the l.h.s. is the (known) SFR function, while under the integral on the r.h.s. the first factor is the cosmic time derivative of the (unknown) stellar mass function minus a source term due to dry mergers (i.e., adding the entire mass content in the stars of merging objects without contributing significantly to in situ star formation), and the second factor is the overall time spent by a galaxy in an SFR bin obtained from the star formation history. The interested reader can find in Aversa et al. (2015) an extended discussion of how and under which hypothesis the standard differential form of the continuity equation is recovered.

In general, the continuity equation above is an integro-differential and has to be solved numerically. If the source term due to dry merging is negligible (as it indeed turns out to be for $z \gtrsim 1$ according to simulations; see Section 3.1 for details) and the star formation histories have simple shapes as in Equations (3) and (5), the continuity equation can be solved analytically along the following lines (see Aversa et al. 2015). First, the time lapses spent by the galaxy in a logarithmic bin of the SFR read

$$\begin{aligned}\frac{d\tau}{d\log\dot{M}_\star}(\dot{M}_\star|M_\star, t) &= \frac{1}{\kappa(\kappa+1)^{1/\kappa}}\,\frac{\dot{M}_\star^{1/\kappa}}{M_\star^{1/\kappa}}\,\tau_{\rm sphe}^{1+1/\kappa} \\ &\times \ln(10)\,\Theta_{\rm H}\left[\dot{M}_\star \leqslant \frac{(\kappa+1)M_\star}{(1-\mathcal{R})\tau_{\rm sphe}}\right], \\ &= \tau_{\rm disc}\,\ln(10)\,\Theta_{\rm H}\left[\dot{M}_\star \leqslant \frac{M_\star}{(1-\mathcal{R})\tau_{\rm disc}}\right]\end{aligned} \tag{7}$$

for galaxies with spheroid- and disk-like star formation histories, respectively. In both expressions, the Heaviside step function $\Theta_{\rm H}(\cdot)$ specifies the maximum SFR contributing to a given final stellar mass.

Inserting these expressions into the continuity equation, Equation (6), and differentiating with respect to $\dot{M}_\star$ and then integrating over cosmic time yield the closed-form solutions

$$\begin{aligned}\frac{dN(\log M_\star, t)}{d\log M_\star} &= -\kappa(1+\kappa)^{1/\kappa}\,M_\star^{1/\kappa}\int_0^t dt'\frac{\partial_{\ln\dot{M}_\star}}{f_{\tau_{\rm sphe}}} \\ &\left[\dot{M}_\star^{-1/\kappa}\,\tau_{\rm sphe}^{-1-1/\kappa}\,\frac{dN}{d\log\dot{M}_\star}(\dot{M}_\star, t')\right]_{|\dot{M}_\star=\frac{(1+\kappa)M_\star}{(1-\mathcal{R})\tau_{\rm sphe}}}; \\ &= -\int_0^t dt'\frac{\partial_{\ln\dot{M}_\star}}{f_{\tau_{\rm disc}}}\left[\tau_{\rm disc}^{-1}\,\frac{dN}{d\log\dot{M}_\star}(\dot{M}_\star, t')\right]_{|\dot{M}_\star=\frac{M_\star}{(1-\mathcal{R})\tau_{\rm disc}}},\end{aligned} \tag{8}$$

again for galaxies with spheroid- and disk-like star formation histories, respectively; in both expressions, we used the shorthand $f_\tau \equiv 1 + \partial_{\log\dot{M}_\star}\log\tau$, which is not trivially equal to one when τ depends explicitly on the SFR (as in Equation (4)). The above equation is numerically solved on a grid in $M_\star$ and z (or cosmic time t_z). We use a grid of 100 equally spaced points in $\log M_\star[M_\odot]$ within the range [8, 13] and a grid of 1000 equally spaced points in redshift z within the range [0, 20]; for optimal interpolation, the SFR functions and the star formation timescales were defined on the same grid of redshifts and on a grid of 100 equally spaced points in $\log\dot{M}_\star[M_\odot\,{\rm yr}^{-1}]$ within the range $[-2, 4]$.

3.1. Dry merging

In the presence of mergers, the source $S(M_\star, t) = S_+ - S_-$ actually includes the difference between a creation S_+ and a destruction S_- term. The former depends on the merger rate of objects with smaller masses into the descendant mass $M_\star$, while the latter depends on the merger rates of the mass $M_\star$ into more

massive objects. Given the merger rate $dN_{\rm merg}/d\log M_\star\, d\mu\, dt$ for the production of a descendant mass $M_\star$ by the merging of two progenitors with (smaller to higher) mass ratio μ, the creation term reads

$$S_+(M_\star, t) = \frac{1}{2}\int_{\mu_{\rm min}}^1 d\mu\, \frac{dN_{\rm merg}}{d\log M_\star\, d\mu\, dt}(M_\star, \mu, t), \quad (9)$$

while the destruction term is written

$$S_-(M_\star, t) = \frac{1}{2}\int_{\mu_{\rm min}}^1 d\mu \left[\frac{dN_{\rm merg}}{d\log M_\star\, d\mu\, dt}(M_\star(1+\mu)/\mu, \mu, t) + \frac{dN_{\rm merg}}{d\log M_\star\, d\mu\, dt}(M_\star(1+\mu), \mu, t)\right]. \quad (10)$$

In the above, $\mu_{\rm min}$ is the minimum mass ratio of the progenitors; typically, $\mu_{\rm min} = 0.3$ includes only "major mergers," 0.1 includes major and minor mergers, and $\lesssim$0.1 practically includes all mergers. We take $\mu_{\rm min} = 0.01$ in the following.

The outcomes of the Illustris simulations by Rodriguez-Gomez et al. (2015, 2016), who provide a handy fitting function for the merger rate per descendant galaxy, form our basis:

$$\frac{dn_{\rm merg}}{d\mu\, dt}(M_\star, \mu, t) = A(z)\left(\frac{M_\star}{10^{10}\, M_\odot}\right)^{\omega(z)} \times \left[1 + \left(\frac{M_\star}{2\times 10^{11}\, M_\odot}\right)^{\delta(z)}\right]\mu^{\beta(z)+\gamma\,\log(M_\star/10^{10}\, M_\odot)}, \quad (11)$$

where

$$A(z) = A_0(1+z)^\eta\,,\ \omega(z) = \omega_0(1+z)^{\omega_1}\,,$$
$$\beta(z) = \beta_0(1+z)^{\beta_1},\ \delta(z) = \delta_0(1+z)^{\delta_1} \quad (12)$$

with $A_0 \approx 10^{-2.2287}\,{\rm Gyr}^{-1}$, $\eta \approx 2.4644$, $\omega_0 \approx 0.2241$, $\omega_1 \approx -1.1759$, $\beta_0 \approx -1.2595$, $\beta_1 \approx 0.0611$, $\gamma \approx -0.0477$, $\delta_0 \approx 0.7668$, and $\delta_1 \approx -0.4695$. The above authors have validated this expression against various data sets, including observations of galaxy pairs. Two remarks are in order here. First, we caution that at $z \gtrsim 1$, the Illustris simulation does not perfectly reproduce the observed galaxy stellar mass function; however, this does not concern much the merger rates, since as we shall demonstrate, the growth in stellar mass at high redshift is mainly dominated by in situ star formation. Second, our results will turn out to be robust against other choices of the merger rate; we checked this by exploiting the galaxy merger rates extracted from the hydrodynamic simulations by Stewart et al. (2009) and the halo merger rates based on the N-body simulation by Fakhouri et al. (2010) coupled with empirical relationships connecting halo and stellar mass (e.g., Moster et al. 2013).

Multiplying the merger rates above by the stellar mass function yields the quantity

$$\frac{dN_{\rm merg}}{d\log M_\star\, d\mu\, dt}(M_\star, \mu, t) = \frac{dn_{\rm merg}}{d\mu\, dt}(M_\star, \mu, t)\frac{dN}{d\log M_\star\, dt}(M_\star, t), \quad (13)$$

which enters the source terms in Equations (9) and (10). As discussed by Rodriguez-Gomez et al. (2015, 2016), the above expression also takes into account stellar mass stripping from satellites prior to dry mergers. Plainly, when merging is introduced, the continuity equation becomes fully integro-differential and must be solved numerically. We computed the full solution and found that, to a good approximation, one can solve the problem iteratively, using Equation (8) as the zeroth order solution and then updating it with the correction due to the merging terms.

3.2. Cosmic Stellar Mass Density and the Soltan Argument

Once the redshift-dependent stellar mass function is known, the cosmic stellar mass density is obtained as

$$\rho_{M_\star}(t) \equiv \int d\log M_\star M_\star \frac{dN}{d\log M_\star}(M_\star, t)\,, \quad (14)$$

where the integration is typically performed over stellar masses above $10^8\, M_\odot$ for fair comparison with observational determinations (see discussion by Madau & Dickinson 2014).

Interestingly, if $\tau_{\rm sphe,disc}$ is independent of, or only weakly dependent on $\dot M_\star$, a Soltan (1982) argument holds for the stellar content of galaxies (see Aversa et al. 2015); classically, this connects the cosmic luminosity density to the relic mass density of a population via an average conversion efficiency. In the present context, the Soltan argument can be easily found by multiplying both sides of Equation (6) by $\dot M_\star$ and integrating over it and over cosmic time to obtain

$$\rho_{M_\star} = (1-\mathcal{R})\int_0^t dt' \int d\log \dot M_\star \dot M_\star \frac{dN}{d\log \dot M_\star}(\dot M_\star, t')\,. \quad (15)$$

We highlight here that the IMF-dependent factor $1-\mathcal{R}$ plays the role of radiative efficiency in the classic Soltan argument for black holes. Note that for conventional IMFs, most of the stellar mass in galaxies reside in stars with mass $\lesssim 1\, M_\odot$; since these stars emit most of their luminosity in the near-IR, the galaxy stellar mass $M_\star$ can be inferred from the near-IR luminosity functions. On the other hand, the SFR function is determined from UV and far-IR/submillimeter/radio observations, as discussed in Section 2. Thus, in principle, accurate determinations of the SFR and stellar mass functions in these independent manners could be exploited via the Soltan argument above to constrain the average galaxy IMF at different redshifts. In practice, however, the dependence on the IMF is weak, and current observational uncertainties do not allow this program to be fulfilled right now.

3.3. Star Formation Efficiency

We now connect the stellar mass function to the underlying, gravitationally dominant DM component, with the aim of deriving the star formation efficiency $f_\star \equiv M_\star/f_{\rm b}\, M_{\rm H}$. This represents the fraction of the baryonic mass $f_{\rm b}\, M_{\rm H} \approx 0.16\, M_{\rm H}$ initially associated with a DM halo of mass $M_{\rm H}$ that has been eventually converted into stars. For this purpose, we exploit the abundance-matching technique, a standard way of deriving a

monotonic relationship between galaxy and halo properties by matching the corresponding integrated number densities (e.g., Vale & Ostriker 2004; Shankar et al. 2006; Behroozi et al. 2013; Moster et al. 2013).

For a fair comparison with the determination of the star formation efficiency $f_\star \equiv M_\star/f_{\rm b}\,\langle M_{\rm H}\rangle$ via weak gravitational lensing (e.g., Velander et al. 2014; Hudson et al. 2015; Mandelbaum et al. 2016) and galaxy kinematics (e.g., More et al. 2011; Wojtak & Mamon 2013), which are based on galaxy samples selected by stellar mass, we aim at deriving the average halo mass $\langle M_{\rm H}\rangle\,(M_\star, z)$ associated with a given $M_\star$. In the abundance-matching formalism, this relationship is obtained via the equation (see Aversa et al. 2015 for details)

$$\int_{\log\langle M_{\rm H}\rangle\,(M_\star,z)}^{\infty} d\log M'_{\rm H}\,\frac{dN}{d\log M_{\rm H}}(M'_{\rm H},\,z) = \int_{-\infty}^{+\infty} d\log M'_\star\,\frac{dN}{d\log M_\star}(M'_\star,\,z)\,\frac{1}{2}\,{\rm erfc}\left\{\frac{\log[M_\star/M'_\star]}{\sqrt{2}\;\sigma_{\log M_{\rm H}}}\right\}, \quad (16)$$

which holds when a log-normal distribution of $M_{\rm H}$ at a given $M_\star$ with dispersion $\sigma_{\log M_{\rm H}}$ is assumed.

We follow previous studies based on various semiempirical methods of galaxy and halo connection (see Rodriguez-Puebla et al. 2015, their Figure 10) and adopt $\sigma_{\log M_{\rm H}} \approx \max\,[0.05,\,0.05 + 0.15(\log M_\star[M_\odot] - 10)]$ for $\log M_\star[M_\odot]$ within the range [8.5, 12.5]. In Equation (16), the quantity $dN/d\log M_{\rm H}$ is usually taken as the halo mass function from N-body simulations (e.g., Tinker et al. 2008; Watson et al. 2013; Bocquet et al. 2016; Comparat et al. 2017), which includes galaxy groups and clusters. This is particularly suitable when comparing with observational determinations of the star formation efficiency based on weak gravitational lensing (see references above), which integrate all of the DM mass along the line of sight, including that associated with the surrounding galaxy environment.

However, in order to infer the star formation efficiency of individual galaxies and not of a galaxy system like a group or a cluster, it would be more appropriate to use the galaxy halo mass function, i.e., the mass function of halos hosting one individual galaxy. This can be built up from the overall halo mass function by adding to it the contribution of subhalos and by probabilistically removing from it the contribution of halos corresponding to galaxy systems via the halo occupation distribution modeling. We refer the reader to Appendix A of Aversa et al. (2015) for details on such a procedure.

3.4. Galaxy Main Sequence

The vast majority of galaxies is endowed with stellar masses strongly correlated with the ongoing SFR, in the way of an almost linear relationship dubbed the "Main Sequence," with a normalization steadily increasing as a function of redshift and with a limited scatter around 0.25 dex (see Daddi et al. 2007; Rodighiero et al. 2011, 2015; Speagle et al. 2014; Whitaker et al. 2014; Renzini & Peng 2015; Salmon et al. 2015; Tasca et al. 2015; Kurczynski et al. 2016; Tomczak et al. 2016; Bourne et al. 2017; Dunlop et al. 2017; Schreiber et al. 2017).

We exploit the abundance matching between the SFR functions (Figure 1) and the stellar mass functions (Figure 4) self-consistently derived from the continuity equation (see Equation (6)) to compute the average SFR $\langle\dot M_\star\rangle\,(M_\star, z)$ associated with a given stellar mass $M_\star$. This reads

$$\int_{\log\langle\dot M_\star\rangle\,(M_\star,z)}^{\infty} d\log\dot M'_\star\,\frac{dN}{d\log\dot M_\star}(\dot M'_\star,\,z) = \int_{-\infty}^{+\infty} d\log M'_\star\,\frac{dN}{d\log M_\star}(M'_\star,\,z)\,\frac{1}{2}\,{\rm erfc}\left\{\frac{\log[M_\star/M'_\star]}{\sqrt{2}\;\sigma_{\log\dot M_\star}}\right\}, \quad (17)$$

which holds when a log-normal distribution of $\dot M_\star$ at a given $M_\star$ with dispersion $\sigma_{\log\dot M_\star} \approx 0.15$ dex is adopted (see Aversa et al. 2015).

The comparison of the resulting main sequence with the observational data will actually constitute an additional constraint on the assumed star formation histories for individual galaxies (see Equations (3) and (5)), on the star formation timescales and the associated scatter, and on the robustness of our results to other aside assumptions discussed in previous sections.

4. Results

In Figure 4, we present the stellar mass function at different redshifts obtained via the continuity equation, including both in situ star formation and (dry) mergers. We highlight the average result with solid lines, and the 1σ dispersion expected from the scatter in the star formation timescales and merging histories as shaded areas (see Section 2 for details). We compare our results to recent observational data (Tomczak et al. 2014; Grazian et al. 2015; Moffett et al. 2016; Song et al. 2016; Thanjavur et al. 2016; Bernardi et al. 2017; Davidzon et al. 2017), finding excellent agreement.

We stress that in situ star formation within galaxies dominates over dry mergers in building up the stellar mass function at high redshifts, all the way down to $z \sim 1$, while at lower redshifts, $z \lesssim 1$, dry mergers can contribute appreciably to the stellar mass growth. This is highlighted when comparing the solid and dashed lines in Figure 4, which illustrate the mass function at different redshifts when including or excluding dry mergers, respectively (the two sets of curves are actually superimposed for $z \gtrsim 1.5$). The effect of dry mergers on the stellar mass function is twofold: the number of low-mass galaxies is decreased appreciably because of the merging into larger units, whereas the high-mass end of the stellar mass function is boosted toward larger masses because of mass additions from smaller objects; dry mergers mainly affect the most massive galaxies that are typically dominated by the spheroidal component. Such a picture is in agreement with what is recently emerging from state-of-the-art numerical simulations (see Schaye et al. 2015; Rodriguez-Gomez et al. 2016), semiempirical models (see Behroozi et al. 2013), and analysis of observations based on density-matching arguments (see Hill et al. 2017).

The dotted lines show the contribution to the stellar mass function from galaxies with a spheroid-like star formation

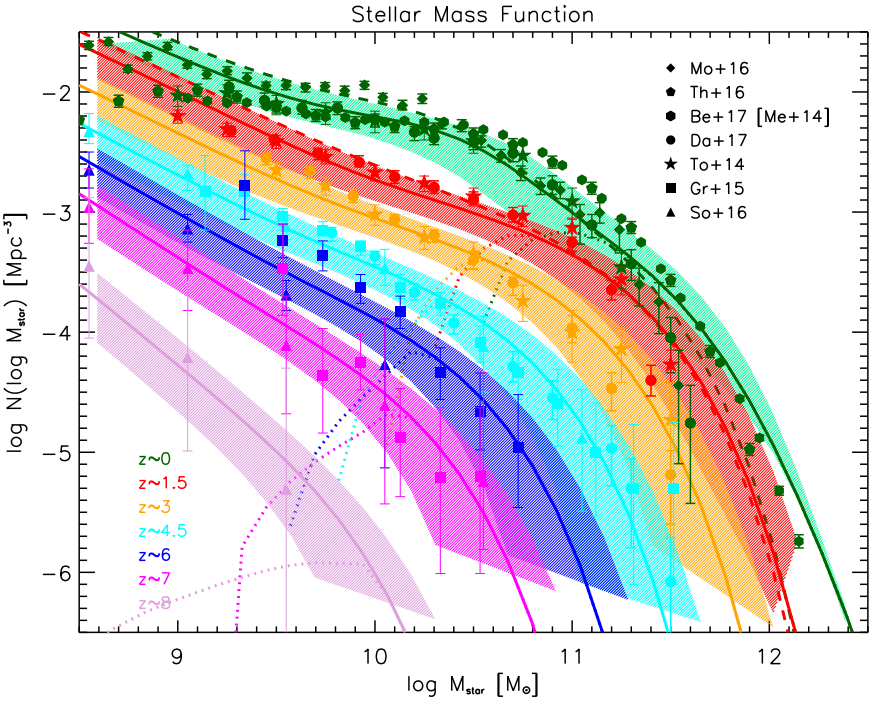

Figure 4. Stellar mass function at redshifts $z = 0$ (green), 1.5 (red), 3 (orange), 4.5 (cyan), 6 (blue), 7 (magenta), and 8 (lilac), determined via the continuity equation including both in situ star formation and dry mergers (solid lines); shaded areas represent the 1σ uncertainty resulting from the scatter in star formation timescales (see Section 2 for details). Dashed lines (actually superimposed on the solid ones at $z \gtrsim 1.5$) refer to the outcome of including only the in situ star formation, and dotted lines show the contribution to the stellar mass function from galaxies with spheroid-like star formation histories that featured SFRs exceeding $100\,M_\odot\,\mathrm{yr}^{-1}$. Data are from Moffett et al. (2016; diamonds), Thanjavur et al. (2016; pentagons), Bernardi et al. (2017, based on the M/L ratios by Mendel et al. 2014; hexagons), Davidzon et al. (2017; circles), Tomczak et al. (2014; stars), Grazian et al. (2015; squares), and Song et al. (2016; triangles).

history that featured SFRs $\dot{M}_\star \gtrsim 100\,M_\odot\,\mathrm{yr}^{-1}$; this corresponds to the limiting value currently sampled in wide-area far-IR surveys out to $z \lesssim 4$ (e.g., the *Herschel*-ATLAS, see Lapi et al. 2011). It is seen that the descendants of these galaxies populate the high-mass end of the local stellar mass function, and thus are mainly present-day massive dead spheroids (e.g., Moffett et al. 2016). This demonstrates on a statistical basis that strongly star-forming galaxies observed in the far-IR/(sub-)millimeter band constitute the progenitors of massive spheroids. By the same token, we stress that to test at $z \gtrsim 4$ the outcomes of the continuity equation, and better constrain the input SFR functions and the parameters of the star formation history for spheroid progenitors, it will be extremely relevant to improve the accuracy in determining the stellar mass function at the high-mass end for $M_\star \gtrsim$ a few $10^{10}\,M_\odot$ out to $z \lesssim 6$ via wide-area near-IR surveys.

In Figure 5, we focus on the stellar mass function of galaxies with disk-like star formation histories at $z \approx 0$. Our result is in excellent agreement with the observed stellar mass function of disk-dominated galaxies from decomposed data (Moffett et al. 2016; Bernardi et al. 2017); thus, we find a good correspondence between the objects populating the UV-inferred SFR function, to which we assigned disk-like star formation histories, and galaxies with observed disk-dominated morphologies in the stellar mass function. We highlight the fact that disks contribute considerably to the total stellar mass function for stellar masses $M_\star \lesssim$ a few $10^{10}\,M_\odot$, and that the effects of mergers on their stellar mass function are negligible. It is seen from Equation (8) that the observed steepness for $M_\star \gtrsim$ a few $10^{10}\,M_\odot$ in the local stellar mass function of disk-dominated galaxies mirrors that in the input UV-inferred SFR functions at $z \lesssim 1$. We caveat that assigning a disk-like star formation history (with long star formation timescales) even to objects populating the UV+far-IR/submillimeter/radio SFR functions at $z \lesssim 1$ would considerably overproduce the number of massive disks; this is because the UV+far-IR/submillimeter/radio functions are much higher than the UV-inferred ones at a given SFR. In fact, the UV+far-IR/submillimeter/radio SFR functions at $z \lesssim 1$ must be populated by objects with spheroid-like star formation history; the continuity equation shows these star formation events to change little the total stellar mass function at $z \sim 0$ with respect to that at $z \sim 1$, mildly affecting the number density of galaxies with $M_\star \gtrsim 10^{10}\,M_\odot$.

In Figure 6, we show how our resulting stellar mass function depend on the input SFR function and on the parameters of the star formation history. To highlight such dependencies in simple terms, it is convenient to assume a piecewise power-law shape of the SFR function $dN/d\log\dot{M}_\star \propto \dot{M}_\star^{-\chi}$, with $\chi \lesssim 1$ at the faint and $\chi > 1$ at the bright end. Then, it is easily seen from Equation (6) that the resulting stellar mass function (in the absence of mergers) behaves as

$$\frac{dN}{d\log M_\star} \propto \frac{1+\kappa\,\chi}{(1+\kappa)^\chi}\,(1-\mathcal{R})^{\chi+1/\kappa}\,M_\star^{-\chi}\,\tau_{\rm sphe}^{\chi-1} \propto \chi\,(1-\mathcal{R})^\chi\,M_\star^{-\chi}\,\tau_{\rm disc}^{\chi-1} \quad (18)$$

for galaxies with spheroid-like and disk-like star formation histories, respectively. Thus, the stellar mass function features an almost direct dependence on the star formation timescales

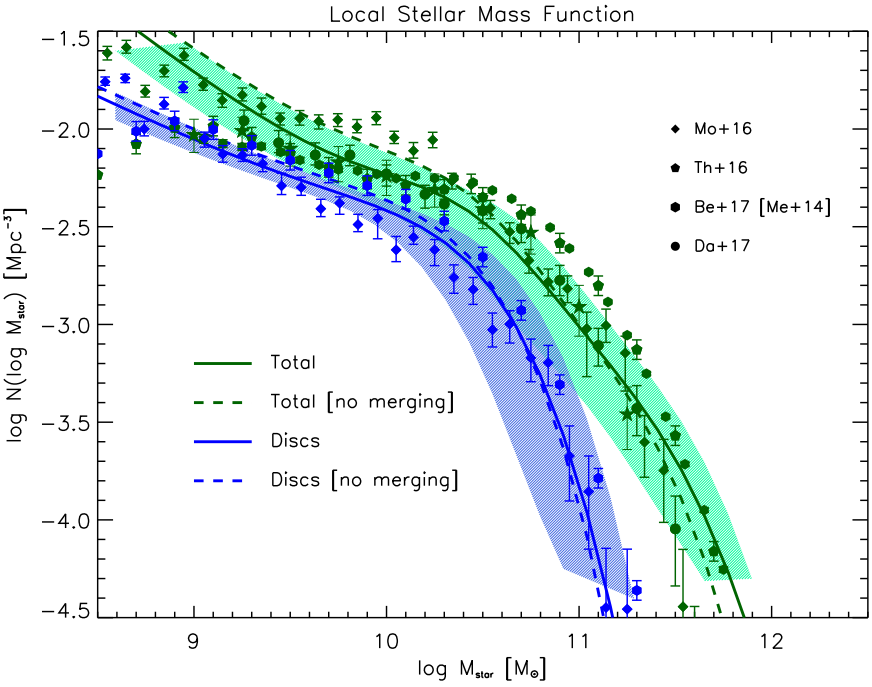

Figure 5. Stellar mass function at redshifts $z = 0$. The green solid line and shaded area refer to the total galaxy population (average and 1σ uncertainty), while the blue solid lines and shaded area refer to galaxies with disk-like star formation history. The dashed lines highlight the outcomes without including dry mergers (see Section 3.1 for details). Data are from Moffett et al. (2016; diamonds), Thanjavur et al. (2016; pentagons), Bernardi et al. (2017, based on the M/L ratios by by Mendel et al. 2014; hexagons), and Davidzon et al. (2017; circles).

$\tau_{\rm sphe,disc}$ at the high-mass end, which is mostly contributed by high SFRs where $\chi > 1$; on the other hand, the dependence is inverse but mild at the low-mass end, mainly contributed by low-SFR galaxies with $\chi \lesssim 1$; note, however, that the value of the SFR where χ appreciably exceeds unity is much lower for the UV-inferred than for the UV+far-IR/submillimeter/radio SFR functions. The dependence on the parameter κ entering the star formation history $\dot{M}_\star(\tau) \propto \tau^\kappa$ is mild, direct at the low-mass end and inverse at the high-mass end. The dependence on the IMF is encapsulated in the restituted fraction $1 - \mathcal{R}$ and in the factor used to convert the observed UV+far-IR/submillimeter/radio luminosity function into the SFR function, e.g., passing from the Chabrier to the Salpeter (1955) IMF, the high-mass end of the stellar mass function is increased somewhat, while a strong suppression is originated when based on a top-heavy IMF (e.g., Lacey et al. 2010). Finally, adopting an SMC extinction law in place of the Calzetti law to determine input SFR function amounts to altering somewhat the exponent χ, and thus changes little the final outcome of the stellar mass function; on the other hand, adopting the UV-inferred SFR function at any redshift (i.e., neglecting far-IR/submillimeter/radio data) would imply that the stellar mass function for large stellar masses (see discussion by Mancuso et al. 2016a, 2016b) that are indeed built up in dusty star-forming galaxies with violent SFRs is strongly underestimated.

In Figure 7, we focus on the stellar mass function of quiescent (passively evolving) galaxies; these systems have been increasingly observed with appreciable number density out to high redshift $z \lesssim 4$ after selection via color–color diagrams in deep near-IR surveys (see Tomczak et al. 2014; Davidzon et al. 2017; Glazebrook et al. 2017; Lonoce et al. 2015). Typically, these selections tend to pick up galaxies that have been quenched since, and then passively evolving over, a quiescence time interval $\Delta t_{\rm qui} \sim 250$–$500$ Myr. Thus, we compute the associated stellar mass function from the continuity equation by replacing the upper limit of integration in Equation (6) with $\tau_{\rm sphe}$–$\Delta t_{\rm qui}$. The result for two different values of $\Delta t_{\rm qui} \approx 250$ and 500 Myr agrees very well with the observational determinations out to $z \lesssim 4$. Plainly, a higher quiescence time $\Delta t_{\rm qui}$ implies a lower mass function, especially toward higher redshift where the cosmic time is smaller and progressively closer to $\tau_{\rm sphe}$. The decrease of the mass function at the low-mass end is due to the fact that small galaxies are still actively forming stars, since they feature longer star formation timescales; as a consequence, the fraction of galaxies in passive evolution decreases rapidly with stellar mass. The downturn shifts toward larger masses toward higher z, passing from 10^{10} to a few $10^{10}\,M_\odot$ from $z \approx 0$ to $z \gtrsim 3$.

In Figure 8, we show the cosmic stellar mass density, obtained according to Equation (15). Our result from integrating the overall stellar mass function from the continuity equation is compared with the data collection by Madau & Dickinson (2014) and with the recent estimates by Song et al. (2016) and Davidzon et al. (2017) at high redshift. The agreement between our results and the data is remarkably good. We also highlight the contribution to the total stellar mass density from galaxies with disk-like and spheroid-like star formation histories; the latter dominates the overall mass density at any redshift, though at $z \lesssim 1$ disks brings an appreciable contribution of around 40%. Note that the fraction of galaxies that are quiescent (here we use $\Delta t_{\rm qui} \approx 250$ Myr; see the above discussion), which are basically massive spheroids, constitute only a fraction, 50%, of the total mass density (contributed also by small spheroids/irregulars and disks that are still active) in the local universe and rapidly

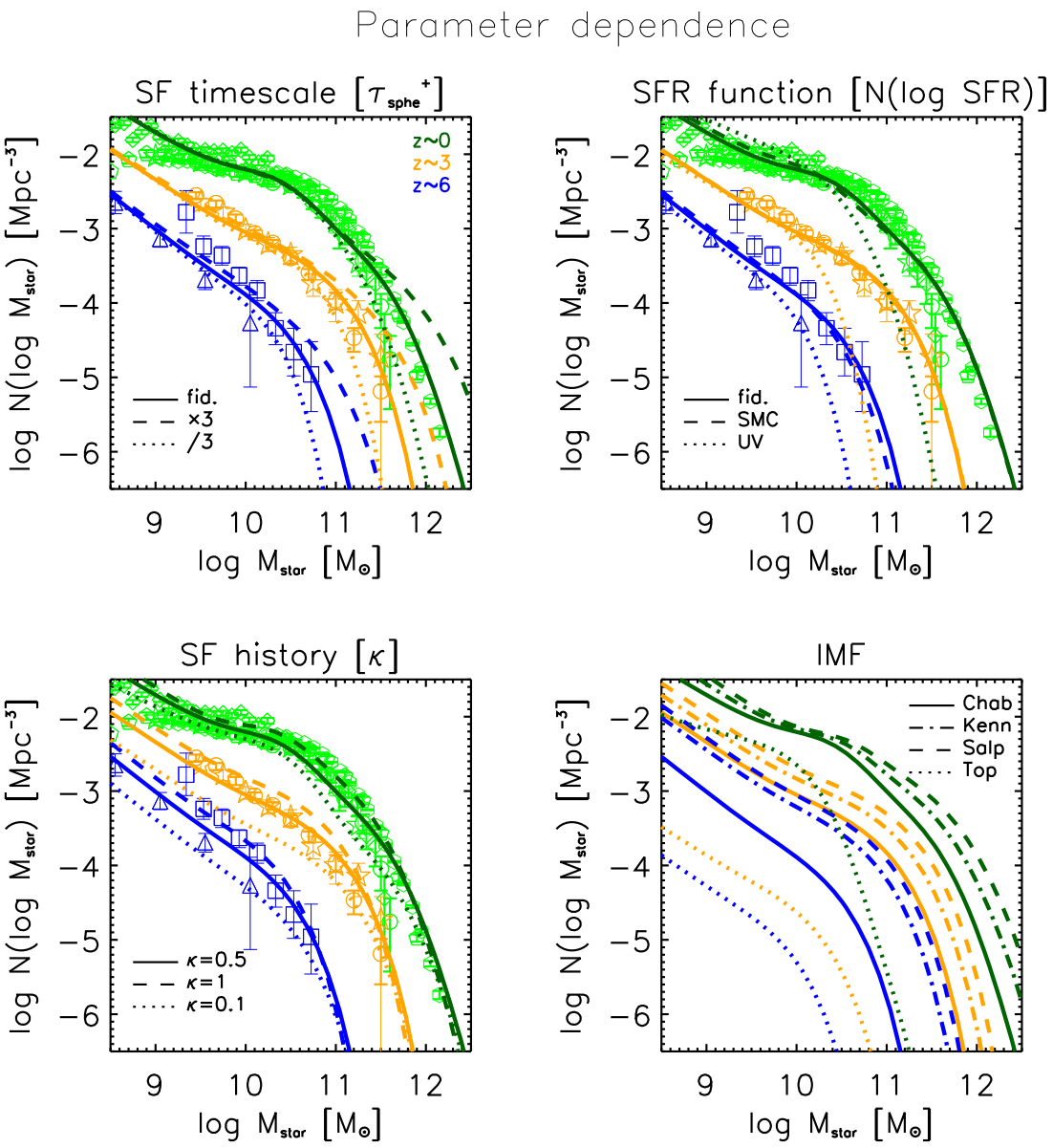

Figure 6. Parameter dependence of the stellar mass function at redshifts $z = 0$ (green), 3 (orange), and 6 (blue); data as in Figure 4. Top-left panel: dependence on the star formation timescale $\tau_{\rm sphe}^{+}$; solid lines refer to the fiducial value in Equation (4), dashed lines to a value three times higher, and dotted lines to a value three times lower. Bottom-left panel: dependence on the parameter κ in the star formation history of Equation (3); solid lines refer to the fiducial value $\kappa = 0.5$, dashed lines to $\kappa = 1$, and dotted lines to $\kappa = 0.1$. Top-right panel: dependence on the input SFR function; solid lines refer to the fiducial one represented in Figure 1, dashed lines to that derived assuming an SMC (in place of the Calzetti) extinction law, dotted line to that inferred from pure UV-dust-corrected data (i.e., neglecting far-IR/submillimeter/radio data). Bottom-right panel: dependence on the IMF (data are not plotted for clarity); solid lines refer to the fiducial Chabrier IMF, dotted–dashed lines to the Kennicutt (1983) IMF, dashed lines to the Salpeter (1955) IMF, and dotted lines to a top-heavy IMF (as in Lacey et al. 2010).

declines to values $\lesssim$10% at higher redshift $z \gtrsim 2$. The overall shape agrees well with the estimates by Muzzin et al. (2013), Straatman et al. (2014), and Davidzon et al. (2017).

For reference, in the figure we also report the mass density (scaled down by a factor 10^{-2}) of galaxy halos with mass $M_{\rm H} \gtrsim 10^{8.5}\,M_\odot$, the minimum threshold for efficient star formation required to solve the missing satellite problem (see Boylan-Kolchin et al. 2014; Wetzel et al. 2016; Lapi et al. 2017). The evolution in halos and in the stellar mass content of galaxies differs both in shape and in normalization; these differences stem from the inefficiency of galaxy formation due to feedback processes (e.g., supernovae, stellar winds, active galactic nuclei); the decrease at high z in the number density of massive halos, which are the hosts of the most massive galaxies; and the inability to grow massive galaxies at high redshift since the growth timescales become comparable to the age of the universe.

In Figure 9, we show the star formation efficiency, computed according to Equation (16). The green solid line and shaded area illustrate the outcome when matching the total stellar mass function from the continuity equation to the overall halo mass function at $z \approx 0$; note that the shaded area takes into account the uncertainty in the determination of the local stellar mass function from the continuity equation and that arising from the rather flat shape of the average $\langle M_{\rm H}\rangle(M_\star)$ correlation at the high-mass end. Our result is compared with the local data for early- and late-type galaxies from various authors, determined via weak lensing (see Velander et al. 2014; Hudson et al. 2015;

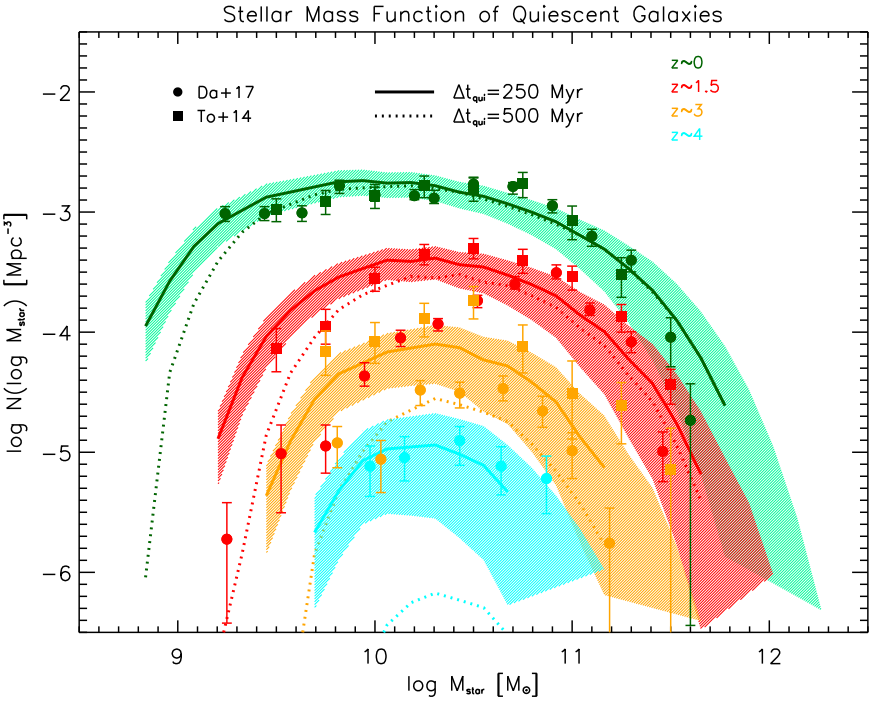

Figure 7. Stellar mass function of quiescent galaxies at redshifts $z = 0$ (green), 1.5 (red), 3 (orange), and 4 (cyan). Solid lines refer to a quiescence timescale of 250 Myr, and dotted lines to 500 Myr (see Section 4 for details). Data are from Davidzon et al. (2017; circles) and Tomczak et al. (2014; squares).

Rodriguez-Puebla et al. 2015; Mandelbaum et al. 2016) and satellite kinematics (see More et al. 2011; Wojtak & Mamon 2013). We stress that the abundance-matching results must be confronted with the data of spheroidal galaxies for the stellar masses above, and with the data of disk-dominated galaxies below, a few $10^{10}\,M_\odot$; this is because spheroids and disks mostly contribute to the local stellar mass function in such stellar mass ranges (see Moffett et al. 2016). Provided these, we find very good agreement within the uncertainties of the respective data sets.

The dotted green line is instead the outcome when matching the local stellar mass function with the galactic halo mass function. This highlights that the decrease in star formation efficiency at large stellar masses is somewhat spurious, being related to the fact that the most massive galaxies tend to live at the center of group/cluster halos, which contain a lot of DM. Considering instead only the DM mass belonging to individual galactic halos would imply that the efficiency stays almost constant or increase somewhat at large masses out to $M_\star \sim 10^{12}\,M_\star$.

The resulting values and shape of the star formation efficiency as a function of stellar mass is easily understood in terms of feedback processes. It is apparent that, because of feedback, galaxy formation is a very inefficient process: at most, 20%–30% of the original baryonic content of halos is converted into stars; this occurs for galaxies with final stellar mass around a few $10^{10}\,M_\odot$ (corresponding to halos with mass $M_{\rm H} \approx 10^{12}\,M_\odot$). At small stellar masses, the action of supernova feedback dominates, while for large stellar masses AGN feedback is likely more relevant; the mass of maximum efficiency corresponds approximately to the transition between the supernova and AGN feedback (see Shankar et al. 2006; Moster et al. 2013; Aversa et al. 2015).

The green dashed line is the outcome of matching the stellar mass function and the overall halo mass function at $z \approx 2$, and it compares well with the efficiencies measured at the same redshift from Hα observations by Burkert et al. (2016). The outcome is also similar, within a factor of 2, to the determination via abundance matching by Moster et al. (2013), Behroozi et al. (2013), and Aversa et al. (2015). The similarity of the efficiency at $z \approx 2$ to the local value is indicative that star formation is mainly an in situ process (see Lilly et al. 2013; Moster et al. 2013; Aversa et al. 2015; Mancuso et al. 2016a).

We also present as a red solid line the outcome of matching the overall halo mass function with the stellar mass function of passively evolving galaxies, again finding a pleasing agreement with the local data for spheroidal galaxies. It is extremely interesting to note that the global efficiency at $z \approx 2$ can be brought on by the efficiency of quiescent galaxies at $z \approx 0$ by allowing (i) the stellar mass to evolve by a factor of 50% due to late star formation or dry mergers (see Rodriguez-Puebla et al. 2015; also Section 3.1), and (ii) the halo mass to evolve by a factor of $4(M_{\rm H}/10^{14}\,M_\odot)^{0.12}$ due to late smooth accretion or tidal stripping (see McBride et al. 2009; Fakhouri et al. 2010; Lapi et al. 2013). We stress that such a result is again indicative of the in situ nature of the star formation in spheroid progenitors and is also extremely relevant for understanding the evolution of the specific angular momentum in galaxies (see Shi et al. 2017).

In Figure 10, we show the main sequence of star-forming galaxies at different redshifts obtained by matching the SFR function and the stellar mass functions from the continuity equation in Equation (17). The outcome at $z \approx 2$ is in pleasing agreement with the observational determination from the large statistics of mass-selected galaxy samples by Rodighiero et al. (2015). This further substantiates our assumed star formation histories for individual galaxies, which are illustrated in three representative cases by red dotted lines; their shapes are dictated by the slowly increasing SFR $\dot{M}_\star \propto \tau^{1/2}$ and

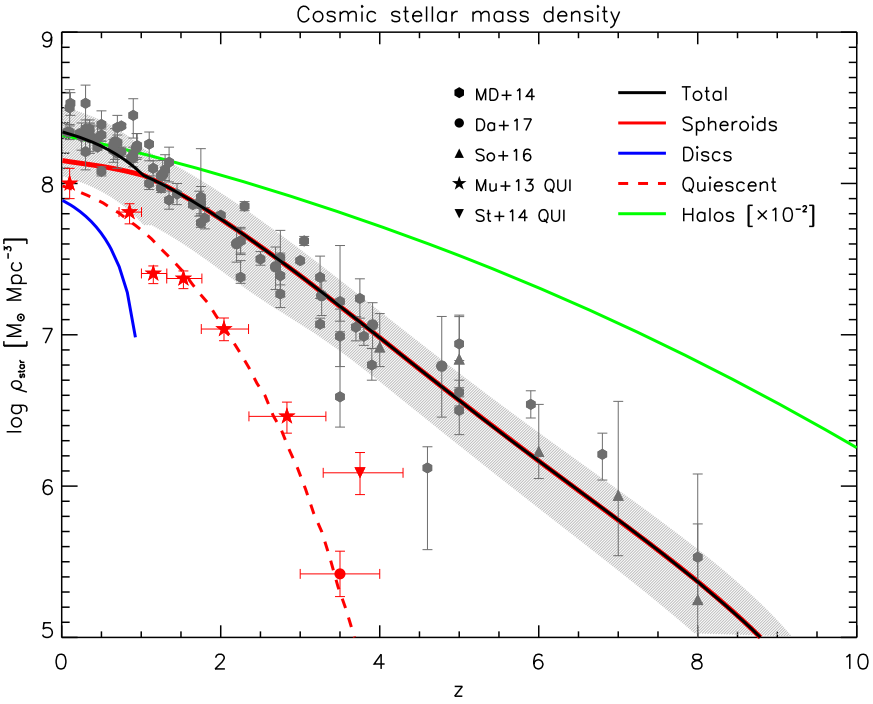

Figure 8. Cosmic stellar mass density as a function of redshift. The black solid line refers to the total galaxy population, blue solid line to galaxies with disk-like star formation histories, red solid line to galaxies with spheroid-like star formation histories, and red dashed line to quiescent galaxies (a quiescence timescale of 250 Myr has been adopted). For reference, the green solid line is the mass density in dark matter halos, scaled down by a factor of 10^{-2}. Data are from Madau & Dickinson (2014), Davidzon et al. (2017; circles), Song et al. (2016; triangles), Muzzin et al. (2013, for quiescent galaxies; stars), and Straatman et al. (2014, for quiescent galaxies; inverted triangles).

appreciably rising stellar mass $M_\star \propto \tau^{3/2}$, which imply $\dot{M}_\star \propto M_\star^{1/3}$. Then, the main sequence corresponds to the portions of such tracks where the galaxies spend most of their lifetime in logarithmic bins of $M_\star$.

To highlight the relevance of observational selections different from that based on stellar mass, in Figure 10 we also report data points for individual, far-IR-selected galaxies by Koprowski et al. (2016), Ma et al. (2016), Negrello et al. (2014), along with Dye et al. (2015), da Cunha et al. (2015), and Dunlop et al. (2017), mainly at redshifts $z \sim 1$–4. An appreciable fraction of the individual, far-IR-selected galaxies around $z \approx 2$ (highlighted in red) lie above the main sequence, i.e., at SFR values higher than expected on the basis of the average relationship at a given $M_\star$. These off-main-sequence objects can be simply interpreted (see Mancuso et al. 2016b) as galaxies caught in an early evolutionary stage and still accumulating their stellar mass. Thus, young star-forming galaxies are found to be preferentially located above the main sequence or, better, to the left of it. As time goes by and the stellar mass increases, the galaxy moves toward the average main-sequence relationship, around which it will spend most of its lifetime. Afterwards, the SFR is quenched by feedback and the galaxy will then evolve passively to become a local early type; it will then populate a region of the SFR versus stellar mass diagram that is substantially below the main sequence. These loci of "red and dead" galaxies are indeed observed locally (see Renzini & Peng 2015) and start to be pinpointed even at high redshift (see Man et al. 2016).

5. Summary

We developed the continuity equation for the stellar mass content of galaxies, and exploited it to derive the stellar mass function of active and quiescent galaxies at redshifts $z \sim 0$–8 from the observed SFR functions and the disk-like or spheroid-like star formation histories for individual galaxies. Our approach based on the continuity equation includes a source term due to dry merging gauged from state-of-the-art numerical simulations and consistent with observations. We then used the abundance-matching technique to investigate the star formation efficiency and the main sequence of star-forming and quiescent galaxies. By comparing these outcomes to current observational estimates, we inferred constraints on the characteristic timescales for star formation and quiescence, on the overall star formation efficiency, and on the amount of stellar mass added by in situ star formation versus that contributed by external (dry) merger events.

Our main findings are the following:

1. We found that the stellar mass function computed from the continuity equation is in excellent agreement with current observational constraints in the extended redshift range $z \sim 0$–8. At high redshift $z \gtrsim 1$, the mass function is produced by galaxies with spheroid-like star formation histories, featuring an approximately constant (or slowly increasing) behavior of the SFR as a function of galactic age; the SFR must last for a time $\tau_{\rm sphe} \approx$ a fraction of a gigayear in strongly star-forming galaxies, while it can proceed over a longer time interval, up to a few gigayears, for less massive objects: this reflects the differential action of supernova and AGN feedback in systems with different mass. We stressed the relevance of using as an input of the continuity equation the SFR function estimated from far-IR/submillimeter/radio, in addition to UV, observations. This is because strongly star-forming galaxies are heavily dust enshrouded, and as

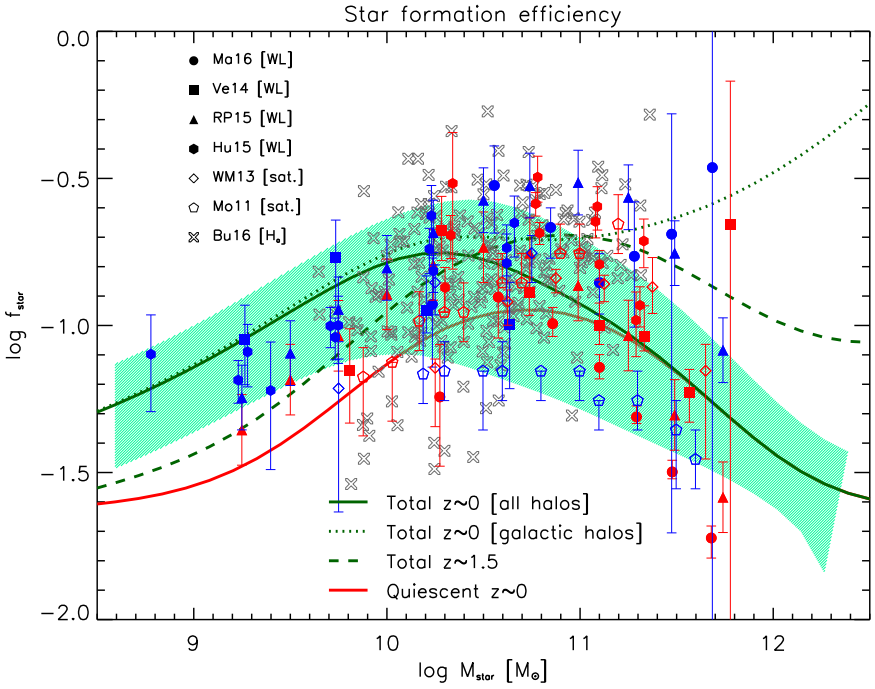

Figure 9. Star formation efficiency $f_\star \equiv M_\star/f_{\rm b}\,\langle M_{\rm H}\rangle$ as a function of the stellar mass $M_\star$, derived from the abundance-matching technique (see Section 3.3 for details). The green solid line and shaded area are the average result and its associated 1σ dispersion at $z\sim 0$ when matching the local stellar mass function to the overall halo mass function; the dotted green line is the result at $z\sim 0$ when matching to the galactic halo mass function; and the dashed green line is the result at $z\sim 1.5$. The solid red line refers to quiescent galaxies at $z\sim 0$. Weak lensing data are from Mandelbaum et al. (2016; circles), Velander et al. (2014; squares), Rodriguez-Puebla et al. (2015; triangles), and Hudson et al. (2015; hexagons); satellite kinematic data are from Wojtak & Mamon (2013; diamonds) and More et al. (2011; pentagons); and H_α data for galaxies at $z\sim 0.8$–2.5 are from Burkert et al. (2016; crosses). Blue symbols are for disk-dominated galaxies and red symbols for spheroids.

such, their intrinsic SFR is considerably underestimated by UV observations, even when corrected for dust extinction according to standard prescriptions based on the UV slope. We highlighted that the mass growth of spheroids is dominated by in situ star formation for $z\gtrsim 1$, while at lower redshifts, dry mergers contribute a mass budget $\lesssim$50%, especially in the most massive objects.

2. At low redshift $z\lesssim 1$, we showed that the stellar mass function of disk-dominated galaxies is well reproduced in our approach when using as input the UV-inferred SFR functions and an exponentially declining SFR history with long characteristic timescales $\tau_{\rm disc}\approx$ several gigayears. On the other hand, we noted that assigning such a disk-like star formation history to the UV+far-IR/submillimeter/radio SFR functions would considerably overproduce the number of massive disks; this is because obscuration is mild in star-forming disks, and so the SFR function from dust-corrected UV data must be effectively exploited as an input of the continuity equation. The effects of mergers on the stellar mass function of disks are negligible.
3. We found that the stellar mass function of quiescent galaxies from the continuity equation is in excellent agreement with current observational constraints for $z\lesssim 4$. We thus demonstrated *quantitatively* via the continuity equation that the dusty, strongly star-forming galaxies recently discovered thanks to wide-area far-IR/submillimeter surveys at $z\gtrsim 1$ are indeed the progenitors of the massive quiescent galaxies increasingly detected out to high redshift $z\lesssim 4$ via deep near-IR surveys. We estimated that the typical time of quiescence (i.e., with absent or negligibly small SFR) for these galaxies is around $\Delta t_{\rm qui}\approx 250$–$500$ Myr. To further test the outcomes of the continuity equation and better constrain the input SFR functions and parameters of the star formation history for individual galaxies, it will be crucial to improve the accuracy in determining the stellar mass function at the high-mass end $M_\star\gtrsim 10^{11}\,M_\odot$ out to $z\lesssim 6$ via wide-area near-IR surveys.
4. We determined the cosmic mass density, finding it to be in excellent agreement with observational determination out to $z\sim 0$–8, both for active and quiescent galaxies. The continuity equation implies an analogue of the Soltan argument for the stellar component, in such a way that the cosmic stellar mass density is by construction consistent with the cosmic time-integrated star formation history, besides a factor depending on the IMF.
5. We determined the star formation efficiency of galaxies as a function of the stellar mass in the local universe, finding it to be in good agreement with diverse observations. We found, in line with previous studies, that the efficiency of star formation is lower than $f_\star\approx 20\%$–30%, with the maximum value being attained around a characteristic stellar mass of a few $10^{10}\,M_\odot$. The behavior as a function of stellar mass can be ascribed to different forms of feedback regulating star formation in galaxies, with supernovae and stellar winds dominating for stellar masses below the characteristic mass, and AGN feedback dominating above it. We also pointed out that the decline of the efficiency for large masses is somewhat spurious, being related to the fact that the most massive galaxies tend to live at the center of group/cluster halos, which contain a lot of DM; considering instead only the

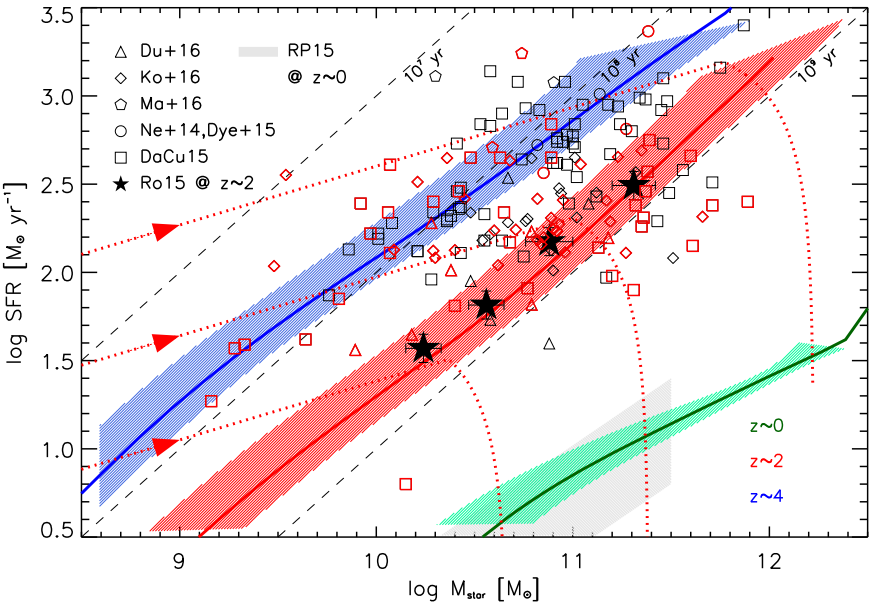

Figure 10. Main sequence of star-forming galaxies. The colored lines are the outcomes (with shaded areas showing the 1σ uncertainty) of matching the SFR function and the stellar mass function from the continuity equation (see Section 3.4 for details), at redshifts $z \approx 0$ (green), 2 (red), and 4 (blue). The red dotted lines show at $z \approx 2$ three evolutionary tracks (the forward time direction indicated by arrows) for individual galaxies with peak values of the SFR around $\dot{M}_\star \approx 20$, 200, and 2000 $M_\odot$ yr^{-1}. The black dashed lines highlight galaxy ages $M_\star/\dot{M}_\star \approx 10^7$, 10^8, and 10^9 yr as labeled. The black filled stars are the observational determinations of the main sequence at $z \approx 2$ based on the statistics of large mass-selected samples by Rodighiero et al. (2015). The other symbols (error bars omitted for clarity) refer to far-IR data for individual objects at $z \sim$ 1–4 (those in the range $z \sim$ 1.5–2.5 are marked in red and the others in black) by Dunlop et al. (2017; triangles), Koprowski et al. (2016; diamonds), Ma et al. (2016; pentagons), Negrello et al. (2014), Dye et al. (2015; circles), and da Cunha et al. (2015; squares). The gray shaded area is the observational estimate at $z \approx 0$ by Renzini & Peng (2015).

DM mass belonging to individual galactic halos would imply that the efficiency stays almost constant or increases somewhat at large stellar masses. Finally, we stressed that the similarity of the efficiency at $z \gtrsim 2$ to the local one is indicative of the early, in situ nature of the star formation process, at least for massive spheroidal galaxies. In fact, we noted that the global efficiency at $z \approx 2$ can be brought on by the global efficiency observed locally for quiescent galaxies by letting the stellar mass to evolve by a modest factor of 50% due to late star formation or dry mergers, and the halo mass to evolve by a factor of a few due to late smooth accretion and/or tidal stripping.

6. We computed the main sequence of star-forming galaxies via abundance matching of the input SFR function and of the stellar mass function self-consistently derived from the continuity equation. We found a remarkable agreement with the observational determinations at different redshifts, thus further constraining our input star formation histories and timescales. We highlighted how off-main-sequence galaxies (located above the average relation) can be simply interpreted in light of our star formation histories as young objects, caught when their stellar mass is still to be accumulated; they will then progressively move onto the main sequence, where they will spend most of their lifetime as active galaxies before being quenched.

Finally, we conclude by stressing that the added value of the continuity equation, developed here on the stellar component of galaxies, is to provide *quantitative*, yet largely *model-independent*, outcomes, to which detailed physical models must comply. In particular, the continuity equation allows the full exploitation of the redshift-dependent SFR functions, stellar mass functions, and galaxy main sequence in order to determine the average star formation histories and timescales of individual galaxies. Our analysis highlights the fact that a bimodal star formation history is required for spheroids and disks: the former must be characterized by a nearly constant SFR over short timescales $\lesssim$ gigayear (increasing somewhat for less star-forming objects), and the latter must feature an SFR exponentially declining over long timescales of several gigayears. Such outcomes of the continuity equation can provide inspiring hints on ways to improve the (subgrid) physical recipes implemented in theoretical models and numerical simulations. Moreover, they can offer a benchmark for forecasts on future observations at very high redshift with multiband coverage of medium and wide areas, as will become routinely achievable with the advent of *JWST*.

We are grateful to J. Beacom, K. Glazebrook, M. Massardi, F. Pozzi, and P. Salucci for stimulating discussions. We thank the referee for a constructive report. This work was partially supported by PRIN MIUR 2015 "Cosmology and Fundamental Physics: Illuminating the Dark Universe with Euclid" and PRIN INAF 2014 "Probing the AGN/galaxy co-evolution through ultra-deep and ultra-high-resolution radio surveys." A.L. acknowledges the RADIOFOREGROUNDS grant (COMPET-05-2015, agreement number 687312) of the European Union Horizon 2020 research and innovation programme.

ORCID iDs

A. Lapi https://orcid.org/0000-0002-4882-1735
A. Bressan https://orcid.org/0000-0002-7922-8440

References

Alavi, A., Siana, B., Richard, J., et al. 2016, ApJ, 832, 56
Aversa, R., Lapi, A., De Zotti, G., Shankar, F., & Danese, L. 2015, ApJ, 810, 74
Barger, A. J., Cowie, L. L., Owen, F. N., et al. 2015, ApJ, 801, 87
Barro, G., Kriek, M., Pérez-González, P. G., et al. 2016, ApJL, 827, L32
Behroozi, P., & Silk, J. 2017, MNRAS, in press, arXiv:1609.04402
Behroozi, P. S., Wechsler, R. H., & Conroy, C. 2013, ApJ, 770, 57
Bernardi, M., Meert, A., Sheth, R. K., et al. 2013, MNRAS, 436, 697
Bernardi, M., Meert, A., Sheth, R. K., et al. 2017, MNRAS, 467, 2217
Bocquet, S., Saro, A., Dolag, K., & Mohr, J. J. 2016, MNRAS, 456, 2361
Bourne, N., Dunlop, J. S., Merlin, E., et al. 2017, MNRAS, 467, 1360
Bouwens, R. J., Aravena, M., De Carli, R., et al. 2016, ApJ, 833, 72
Bouwens, R. J., Illingworth, G. D., Oesch, P. A., et al. 2015, ApJ, 803, 34
Bouwens, R. J., Oesch, P. A., Illingworth, G. D., Ellis, R. S., & Stefanon, M. 2017, ApJ, 843, 129
Boylan-Kolchin, M., Bullock, J. S., & Garrison-Kimmel, S. 2014, MNRAS, 443, L44
Burkert, A., Forster Schreiber, N. M., Genzel, R., et al. 2016, ApJ, 826, 214
Cai, Z.-Y., Lapi, A., Bressan, A., et al. 2014, ApJ, 785, 65
Cai, Z.-Y., Lapi, A., Xia, J.-Q., et al. 2013, ApJ, 768, 21
Calzetti, D., Armus, L., Bohlin, R. C., et al. 2000, ApJ, 533, 682
Caputi, K. I., Ilbert, O., Laigle, C., et al. 2015, ApJ, 810, 73
Cassará, L. P., Maccagni, D., Garilli, B., et al. 2016, A&A, 593, A9
Cavaliere, A., Morrison, P., & Wood, K. 1971, ApJ, 170, 223
Chabrier, G. 2003, ApJL, 586, L133
Chiappini, C., Matteucci, F., & Gratton, R. 1997, ApJ, 477, 765
Citro, A., Pozzetti, L., Moresco, M., & Cimatti, A. 2016, A&A, 592, A19
Comparat, J., Prada, F., Yepes, G., & Klypin, A. 2017, MNRAS, 469, 4157
Conroy, C. 2013, ARA&A, 51, 393
Contini, E., Kang, Xi., Romeo, A. D., & Xia, Q. 2017, ApJ, 837, 27
Cooray, A., Calanog, J., Wardlow, J. L., et al. 2014, ApJ, 790, 40
Coppin, K. E. K., Geach, J. E., Almaini, O., et al. 2015, MNRAS, 446, 1293
Courteau, S., Cappellari, M., de Jong, R. S., et al. 2014, RvMP, 86, 47
Cucciati, O., Tresse, L., Ilbert, O., et al. 2012, A&A, 539, A31
da Cunha, E., Walter, F., Smail, I. R., et al. 2015, ApJ, 806, 110
Daddi, E., Alexander, D. M., Dickinson, M., et al. 2007, ApJ, 670, 173
Davé, R., Rafieferantsoa, M. H., Thompson, R. J., & Hopkins, P. F. 2017, MNRAS, 467, 115
Davidzon, I., Ilbert, O., Laigle, C., et al. 2017, ApJ, in press, arXiv:1701.02734
Diemer, B., Sparre, M., & Torrey, P. 2017, ApJ, 839, 26
Duncan, K., Conselice, C. J., Mortlock, A., et al. 2014, MNRAS, 444, 2960
Dunlop, J. S., McLure, R. J., Biggs, A. D., et al. 2017, MNRAS, 466, 861
Dye, S., Furlanetto, C., Swinbank, A. M., et al. 2015, MNRAS, 452, 2258
Efstathiou, A., Rowan-Robinson, M., & Siebenmorgen, R. 2000, MNRAS, 313, 734
Fakhouri, O., Ma, C.-P., & Boylan-Kolchin, M. 2010, MNRAS, 406, 2267
Finkelstein, S. L., Ryan, R. E., Jr., Papovich, C., et al. 2015, ApJ, 810, 71
Fudamoto, Y., Oesch, P. A., Schinnerer, E., et al. 2017, MNRAS, in press, arXiv:1705.01559
Furlong, M., Bower, R. G., Crain, R. A., et al. 2017, MNRAS, 465, 722
Gallazzi, A., Charlot, S., Brinchmann, J., & White, S. D. M. 2006, MNRAS, 370, 1106
Genzel, R., Forster Schreiber, N. M., Ubler, H., et al. 2017, Natur, 543, 397
Gladders, M. D., Oemler, A., Dressler, A., et al. 2013, ApJ, 770, 64
Glazebrook, K., Schreiber, C., Labbé, I., et al. 2017, Natur, 544, 71
Grazian, A., Fontana, A., Santini, P., et al. 2015, A&A, 575, A96
Gruppioni, C., Calura, F., Pozzi, F., et al. 2015, MNRAS, 451, 3419
Gruppioni, C., Pozzi, F., Rodighiero, G., et al. 2013, MNRAS, 432, 23
Harris, K., Farrah, D., Schulz, B., et al. 2016, MNRAS, 457, 4179
Harrison, C. M., Simpson, J. M., Stanley, F., et al. 2016, MNRAS, 457, L122
Hill, A. R., Muzzin, A., Franx, M., et al. 2017, ApJ, 837, 147
Hopkins, A. M., & Beacom, J. F. 2006, ApJ, 651, 142
Hopkins, P. F., Wetzel, A., Keres, D., et al. 2017, MNRAS, in press, arXiv:1702.06148
Hudson, M. J., Gillis, B. R., Coupon, J., et al. 2015, MNRAS, 447, 298
Ikarashi, S., Ivison, R. J., & Caputi, K. I. 2015, ApJ, 810, 133
Ikarashi, S., Ivison, R. J., Caputi, K. I., et al. 2017, ApJ, 835, 286
Ilbert, O., McCracken, H. J., le Fevre, O., et al. 2013, A&A, 556, A55
Kennicutt, R. C. 1983, ApJ, 272, 54
Kistler, M. D., Yuksel, H., Beacom, J. F., et al. 2009, ApJL, 705, L104
Kistler, M. D., Yuksel, H., & Hopkins, A. M. 2013, arXiv:1305.1630
Koprowski, M., Dunlop, J. S., Michalowski, M. J., et al. 2016, MNRAS, 458, 4321
Koprowski, M. P., Dunlop, J. S., Michalowski, M. J., Cirasuolo, M., & Bowler, R. A. A. 2014, MNRAS, 444, 117
Kriek, M., Conroy, C., van Dokkum, P. G., et al. 2016, Natur, 540, 248
Kurczynski, P., Gawiser, E., Acquaviva, V., et al. 2016, ApJL, 820, L1
Lacey, C. G., Baugh, C. M., Frenk, C. S., et al. 2010, MNRAS, 405, 2
Lapi, A., Gonzalez-Nuevo, J., Fan, L., et al. 2011, ApJ, 742, 24
Lapi, A., Mancuso, C., Celotti, A., & Danese, L. 2017, ApJ, 835, 37
Lapi, A., Raimundo, S., Aversa, R., et al. 2014, ApJ, 782, 69
Lapi, A., Salucci, P., & Danese, L. 2013, ApJ, 772, 85
Leitner, S. N., & Kravtsov, A. V. 2011, ApJ, 734, 48
Leja, J., van Dokkum, P. G., Franx, M., & Whitaker, K. E. 2015, ApJ, 798, 115
Lilly, S. J., Carollo, C. M., Pipino, A., et al. 2013, ApJ, 772, 119
Liu, D., Daddi, E., Dickinson, M., et al. 2017, ApJ, submitted, arXiv:1703.05281
Lonoce, I., Longhetti, M., Maraston, C., et al. 2015, MNRAS, 454, 3912
Ma, J., Gonzalez, A. H., Viera, J. D., et al. 2016, ApJ, 832, 114
Madau, P., & Dickinson, M. 2014, ARA&A, 52, 415
Magnelli, B., Popesso, P., Berta, S., et al. 2013, A&A, 553, A132
Man, A. W. S., Greve, T. R., Toft, S., et al. 2016, ApJ, 820, 11
Mancuso, C., Lapi, A., Prandoni, I., et al. 2017, ApJ, 842, 95
Mancuso, C., Lapi, A., Shi, J., et al. 2016a, ApJ, 823, 128
Mancuso, C., Lapi, A., Shi, J., et al. 2016b, ApJ, 833, 152
Mandelbaum, R., Wang, W., Zu, Y., et al. 2016, MNRAS, 457, 3200
Marconi, A., Risaliti, G., Gilli, R., et al. 2004, MNRAS, 351, 169
Mawatari, K., Yamada, T., Fazio, G. G., Huang, J.-S., & Ashby, M. L. N. 2016, PASJ, 68, 46
McBride, J., Fakhouri, O., & Ma, C.-P. 2009, MNRAS, 398, 1858
Mendel, J. T., Simard, L., Palmer, M., Ellison, S. L., & Patton, D. R. 2014, ApJS, 210, 3
Merloni, A., & Heinz, S. 2008, MNRAS, 388, 1011
Meurer, G. R., Heckman, T. M., & Calzetti, D. 1999, ApJ, 521, 64
Michalowski, M. J., Dunlop, J. S., Koprowski, M. P., et al. 2016, MNRAS, 469, 492
Moffett, A. J., Lange, R., Driver, S. P., et al. 2016, MNRAS, 462, 4336
Mor, R., Netzer, H., Trakhtenbrot, B., Shemmer, O., & Lira, P. 2012, ApJL, 749, L25
More, S., van den Bosch, F. C., Cacciato, M., et al. 2011, MNRAS, 410, 210
Moster, B. P., Naab, T., & White, S. D. M. 2013, MNRAS, 428, 3121
Moustakas, J., Coil, A. L., Aird, J., et al. 2013, ApJ, 767, 50
Mullaney, J. R., Daddi, E., Bethermin, M., et al. 2012, ApJL, 753, L30
Muzzin, A., Marchesini, D., Stefanon, M., et al. 2013, ApJ, 777, 18
Nayyeri, H., Keele, M., Cooray, A., et al. 2016, ApJ, 823, 17
Negrello, M., Amber, S., Amvrosiadis, A., et al. 2017, MNRAS, 465, 3558
Negrello, M., Hopwood, R., Dye, S., et al. 2014, MNRAS, 440, 1999
Netzer, H., Lani, C., Nordon, R., et al. 2016, ApJ, 819, 123
Novak, M., Smolcic, V., Delhaize, J., et al. 2017, A&A, 602, A5
Oesch, P. A., Bouwens, R. J., Carollo, C. M., et al. 2010, ApJL, 725, L150
Page, M. J., Symeonidis, M., Vieira, J., et al. 2012, Natur, 485, 213
Papovich, C., Finkelstein, S. L., Ferguson, H. C., Lotz, J. M., & Giavalisco, M. 2011, MNRAS, 412, 1123
Pezzulli, G., & Fraternali, F. 2016, MNRAS, 455, 2308
Planck Collaboration XIII 2016, A&A, 594, A13
Pope, A., Montana, A., Battisti, A., et al. 2017, ApJ, 838, 137
Reddy, N. A., Kriek, M., Shapley, A. E., et al. 2015, ApJ, 806, 259
Renzini, A. 2006, ARA&A, 44, 141
Renzini, A., & Peng, Y.-J. 2015, ApJL, 801, L29
Riechers, D. A., Daisy Leung, T. K., Ivison, R., et al. 2017, ApJ, submitted, in press arXiv:1705.09660
Rodighiero, G., Brusa, M, Daddi, E., et al. 2015, ApJL, 800, L10
Rodighiero, G., Daddi, E., Baronchelli, I., et al. 2011, ApJL, 739, L40
Rodriguez-Gomez, V., Genel, S., Vogelsberger, M., et al. 2015, MNRAS, 449, 49
Rodriguez-Gomez, V., Pillepich, A., Sales, L. V., et al. 2016, MNRAS, 458, 2371
Rodriguez-Puebla, A., Avila-Reese, V., Yang, X., et al. 2015, ApJ, 799, 130
Romano, D., Silva, L., Matteucci, F., & Danese, L. 2002, MNRAS, 334, 444
Rong, Y., Jing, Y., Gao, L., et al. 2017, MNRAS, 471, L36
Rosario, D. J., Santini, P., Lutz, D., et al. 2012, A&A, 545, 45
Rowan-Robinson, M., Oliver, S., Wang, L., et al. 2016, MNRAS, 461, 1100
Salmon, B., Papovich, C., Finkelstein, S. L., et al. 2015, ApJ, 799, 183
Salpeter, E. E. 1955, ApJ, 121, 161
Salucci, P., Szuszkiewicz, E., Monaco, P., & Danese, L. 1999, MNRAS, 307, 637
Schaye, J., Crain, R. A., Bower, R. G., et al. 2015, MNRAS, 446, 521
Schiminovich, D., Ilbert, O., Arnouts, S., et al. 2005, ApJL, 619, L47

Schreiber, C., Pannella, M., Leiton, R., et al. 2017, A&A, 599, A134
Scoville, N., Aussel, H., Sheth, K., et al. 2014, ApJ, 783, 84
Scoville, N., Sheth, K., Aussel, H., et al. 2016, ApJ, 820, 83
Shankar, F., Lapi, A., Salucci, P., de Zotti, G., & Danese, L. 2006, ApJ, 643, 14
Shankar, F., Weinberg, D. H., & Miralda-Escude, J. 2009, ApJ, 690, 20
Shankar, F., Weinberg, D. H., & Miralda-Escude, J. 2013, MNRAS, 428, 421
Shi, J., Lapi, A., Mancuso, C., Wang, H., & Danese, L. 2017, ApJ, 843, 105
Silva, L., Granato, G. L., Bressan, A., & Danese, L. 1998, ApJ, 509, 103
Simpson, J. M., Smail, I., Swinbank, A. M., et al. 2015, ApJ, 799, 81
Simpson, J. M., Smail, I., Wang, W.-H., et al. 2017, ApJL, 844, L10
Small, T. A., & Blandford, R. D. 1992, MNRAS, 259, 725
Smit, R., Bouwens, R. J., Franx, M., et al. 2012, ApJ, 756, 14
Soltan, A. 1982, MNRAS, 200, 115
Song, M., Finkelstein, S. L., Ashby, M. L. N., et al. 2016, ApJ, 825, 5
Speagle, J. S., Steinhardt, C. L., Capak, P. L., & Silverman, J. 2014, ApJS, 214, 15
Spilker, J. S., Bezanson, R., Marrone, D. P., et al. 2016, ApJ, 832, 19
Stanley, F., Harrison, C. M., Alexander, D. M., et al. 2015, MNRAS, 453, 591
Stewart, K. R., Bullock, J. S., Barton, E. J., et al. 2009, ApJ, 702, 1005
Steinhardt, C. L., Speagle, J. S., & Capak, P. 2014, ApJL, 791, L25
Steinhardt, C. L., Yurk, D., & Capak, P. 2017, MNRAS, 468, 849
Straatman, C. M. S., Labbé, I., Spitler, L. R., et al. 2014, ApJL, 783, L14
Straatman, C. M. S., Labbé, I., Spitler, L. R., et al. 2015, ApJL, 808, L29
Straatman, C. M. S., Spitler, L. R., Quadri, R. F., et al. 2016, ApJ, 830, 51
Strandet, M. L., Weiss, A., Vieira, J. D., et al. 2016, ApJ, 822, 80
Swinbank, M., Harrison, C., Trayford, J., et al. 2017, ApJ, 467, 3140
Tadaki, K.-I., Genzel, R., Kodama, T., et al. 2017, ApJ, 834, 135
Tasca, L. A. M., Le Févre, O., Hathi, N. P., et al. 2015, A&A, 581, A54
Thanjavur, K., Simard, L., Bluck, A. F. L., & Mendel, T. 2016, MNRAS, 459, 44
Thomas, D., Maraston, C., Bender, R., & Mendes de Oliveira, C. 2005, ApJ, 621, 673
Tinker, J. L., Kravtsov, A. V., Klypin, A., et al. 2008, ApJ, 688, 709
Tomczak, A. R., Quadri, R. F., Tran, K. H., et al. 2016, ApJ, 817, 118
Tomczak, A. R., Quadri, R. F., Tran, K.-V. H., et al. 2014, ApJ, 783, 85
Vale, A., & Ostriker, J. P. 2004, MNRAS, 353, 189
van der Burg, R. F. J., Hildebrandt, H., & Erben, T. 2010, A&A, 523, A74
Velander, M., van Uitert, E., Hoekstra, H., et al. 2014, MNRAS, 437, 2111
Wang, R., Wagg, J., & Carilli, C. L. 2013, ApJ, 773, 44
Watson, W. A., Iliev, I. T., D'Aloisio, A., et al. 2013, MNRAS, 433, 1230
Weiss, A., De Breuck, C., Marrone, D. P., et al. 2013, ApJ, 767, 88
Wellons, S., Torrey, P., Ma, C.-P., et al. 2015, MNRAS, 449, 361
Wetzel, A. R., Hopkins, P. F., Kim, J.-H., et al. 2016, ApJL, 827, L23
Whitaker, K. E., Franx, M., Leja, J., et al. 2014, ApJ, 795, 104
Willott, C. J., Bergeron, J., & Omont, A. 2015, ApJ, 801, 123
Wojtak, R., & Mamon, G. A. 2013, MNRAS, 428, 2407
Wyder, T. K., Treyer, M. A., Milliard, B., et al. 2005, ApJL, 619, L15
Xu, L., Rieke, G. H., Egami, E., et al. 2015, ApJ, 808, 159
Yu, Q., & Lu, Y. 2004, ApJ, 602, 603
Yu, Q., & Lu, Y. 2008, ApJ, 689, 732
Zavala, J. A., Montana, A., Hughes, D. H., et al. 2017, NatAs, in press, arXiv:1707.09022